

In Situ Oxidation and Reduction of Cerium Dioxide Nanoparticles Studied by Scanning Transmission Electron Microscopy

Aaron C. Johnston-Peck^{*†}, Wei-Chang D. Yang^{‡#}, Jonathan P. Winterstein[‡], Renu Sharma[‡],
and Andrew A. Herzing^{*†}

[†]Material Measurement Laboratory, National Institute of Standards and Technology,
Gaithersburg, MD 20899, USA

[‡]Center for Nanoscience and Technology, National Institute of Standards and Technology,
Gaithersburg, MD 20899, USA

[#]Maryland NanoCenter, University of Maryland, College Park, MD 20742, USA

*Corresponding Authors:

aaron.johnston-peck@nist.gov (A.C. Johnston-Peck)

andrew.herzing@nist.gov (A.A. Herzing)

Material Measurement Laboratory, National Institute of Standards and Technology, 100 Bureau
Drive Mailstop 8372, Gaithersburg, MD 20899, USA

Abstract

Cerium dioxide nanocubes and truncated octahedra were reduced and oxidized in the scanning transmission electron microscope. The reduction process was stimulated by the electron beam and oxidation was supported by background gases in the microscope environment. High-angle annular dark field imaging is sensitive to local lattice distortions that arise as oxygen vacancies are created and cerium cations reduce enabling high spatial resolution characterization of this process with temporal resolution on the order of seconds. Such measurements enable us to differentiate and infer that the observed behavior between the nanocubes and truncated octahedra may be due to the difference in crystallographic termination of surfaces. In situ measurements taken with different partial pressures of oxygen reveal the cerium oxidation state and the dose rate threshold for the onset of beam reduction are influenced by the environment. Increasing oxygen partial pressure reduces the Ce^{3+} content and decreases susceptibility to electron beam driven reduction.

Keywords

Cerium dioxide; oxidation; reduction; scanning transmission electron microscopy

1. Introduction

In situ scanning transmission electron microscopy (STEM) offers the opportunity to observe materials under dynamic conditions with high spatial resolution. Here we observe the oxidation and reduction of cerium dioxide (CeO_2 , ceria) nanoparticles using STEM and electron energy loss spectroscopy (EELS). CeO_2 is reduced by highly-energetic electron beams. (Garvie and Buseck, 1999) This behavior has been demonstrated to occur when the beam current is increased above a critical dose-rate threshold (Johnston-Peck et al., 2016a). Upon decreasing the beam current, the reduced nanoparticle begins to oxidize through interactions with the background gases in the microscope environment. To study this transformation requires both adequate spatial and temporal resolution. STEM-EELS spectrum imaging has produced datasets quantifying the oxidation state of cerium cations in ceria with atomic spatial resolution (Turner et al., 2011). Unfortunately the dwell time in a spectrum image is typically on the order of milliseconds compared to microseconds for a bright field or annular dark field (ADF)-STEM image. This means the temporal resolution of spectrum imaging is worse for a given set of sampling conditions and would face limitations in tracking dynamic processes. One method to circumvent this limitation is to extract additional information related to the reduction-oxidation (redox) process directly from the ADF images to supplement the EELS data.

To this point, when the sample is oriented to a high-symmetry-crystallographic axis, electron channeling becomes pronounced and local changes in the sample can manifest as contrast within the resulting ADF images. In CeO_2 specifically, atomic static displacements due

to oxygen vacancies and the different ionic radius of Ce^{3+} and Ce^{4+} cations will generate contrast (Johnston-Peck et al., 2016b). The relative simplicity of a single-crystal nanomaterial, without additional features (e.g., line or planar defects) that can also be sources of contrast, presents a situation where the image contrast can be interpreted beyond the mass-thickness relationship of high-angle annular dark field STEM (HAADF-STEM) images to being qualitatively sensitive to relative differences in the extent of reduction. Therefore, in addition to being able to identify different crystallographic phases, we can also discriminate between materials that are the same phase but are anion-deficient (i.e., fluorite CeO_2 and fluorite CeO_{2-x}). This enables tracking of the conversion from CeO_2 to Ce_2O_3 and then back to CeO_2 with a combined temporal and spatial resolution that a spectroscopic technique alone (e.g., STEM-EELS) is currently unable to provide.

With HAADF-STEM imaging we observe nucleation and growth of the cubic sesquioxide phase ($\text{C-Ce}_2\text{O}_3$) in nanocubes, as well as the spatial dependence of the oxidation process in nanocubes and truncated octahedra to CeO_2 from CeO_{2-x} . Analyzing this information along with EELS data we correlate differences in redox activity between particle geometries as a function of surface termination. To appreciate the influence of environment on CeO_2 and the role it plays on the measurement process we measure the critical-dose rate threshold necessary to reduce CeO_2 and quantify Ce^{3+} content as a function of gas pressure using environmental STEM (ESTEM). We observe increasing oxygen pressure affects the results by increasing the critical-dose rate threshold. Also, the Ce^{3+} content of ≈ 5 nm nanoparticles were found to be responsive to environment suggesting that the changes in oxygen chemical potential can influence the outcome of measurements made in the electron microscope.

2. Materials and Methods

Image and EELS data shown in Figures 1-6 and 8a was recorded on an FEI Titan 80-300 equipped with a spherical-aberration corrector for the probe-forming lens. The microscope was operated at an accelerating voltage of 300 kV. The probe convergence angle was ≈ 13.5 mrad; HAADF-STEM images were acquired with collection angles of $\approx (88 \text{ to } 175)$ mrad or $\approx (112 \text{ to } 168)$ mrad. CeO₂ nanocubes were synthesized using wet chemical methods, details can be found in previous reports (Johnston-Peck et al., 2016a; Johnston-Peck et al., 2016b). CeO₂ truncated octahedron and nanoparticles were acquired from Sigma-Aldrich and Strem Chemicals, respectively. Samples were deposited onto a carbon support film and plasma cleaned by a low energy RF plasma (Ar/O₂) to prevent the build-up of amorphous carbon during electron beam irradiation, as a carbon shell inhibits reduction of the CeO₂ particles (Johnston-Peck et al., 2016a).

For irradiation experiments, a 1024 x 1024 raster with a pixel dwell time of 0.8 μs was used. During the EEL spectral acquisition, the electron beam was scanned multiple times over the entire square raster pattern; accordingly, the measurement indicates the spatially-averaged oxidation state of the entire particle. Dose rates ($\text{e}\cdot\text{nm}^{-2}\cdot\text{s}^{-1}$) were calculated by dividing the probe current by the area of the raster. This represents a time-averaged value because each point of the specimen is illuminated only once during each complete raster, not continuously. A value based on the size of the probe would be more representative, however an accurate measurement of the probe profile is challenging and during the experiments the probe profile changes as the current was adjusted. Cumulative doses ($\text{e}\cdot\text{nm}^{-2}$) were calculated by multiplying the dose rate by the exposure time. The electron probe currents were measured using the microscope's fluorescent screen that had been previously calibrated using a pico-ammeter.

EELS data shown in Figures 7 and 8b was recorded on an FEI Titan ESTEM without aberration correction for the probe-forming optics. The microscope is equipped with a residual gas analyzer (RGA). All experiments were conducted using an accelerating voltage of 300 kV. The data shown in Figure 7 was collected with a convergence angle of ≈ 10 mrad. For irradiation experiments, a 1024 x 1024 raster with a per-pixel dwell time of 0.8 μ s was used. During the EEL spectral acquisition, the electron beam scanned multiple times over the entire square raster pattern. The data shown in Figure 8b was collected with a convergence semi-angle of approximately ≈ 3 mrad and a EELS collection angle of ≈ 12.5 mrad and the dispersion was 0.05 eV/ch. A Gatan DualEELS spectrometer was used to acquire the data, to ensure a precise energy-loss scale the zero-loss region and the Ce core-loss region were both recorded. In post-processing, spectra were then aligned relative to the zero-loss peak. The electron probe currents were measured using a pico-ammeter attached to the drift-tube of the EEL spectrometer.

The white-line ratio of the Ce M₅ to the Ce M₄ peak was calculated by taking the second derivative of the spectra and integrating the positive portion of each edge. This was implemented in Digital Micrograph (Mitchell and Schaffer, 2005). The uncertainty of these values is defined as,

$$\delta W = W \sqrt{\left(\frac{\sqrt{N_1}}{N_1}\right)^2 + \left(\frac{\sqrt{N_2}}{N_2}\right)^2}$$

where W is the white-line ratio and N_1 and N_2 are the integrated intensities of the Ce M_{4,5} edges.

Quantification of the EELS data in Figure 8b, whose results are displayed Table 1 was performed by least squares fitting, as employed in EELSModel (Verbeeck and Van Aert, 2004). CeAlO₃:2% Ge and a large-grain CeO₂ powder were used as controls to provide the

characteristic Ce^{3+} and Ce^{4+} spectra. To reduce differences due to sample thickness, the Fourier-Ratio deconvolution, as implemented in Digital Micrograph, was applied. Backgrounds were removed and deconvolution routines were applied to all spectra prior to fitting. The uncertainty of the values reported is the standard deviation of the measurements, where measurements were recorded from multiple regions of each sample.

Simulated images were calculated by the multislice routine using QSTEM (Koch, 2002). Structural information including Debye-Waller factors were obtained from data published by Kümmerle and Heger (Kümmerle and Heger, 1999). Parameters of the simulation approximate the experimental conditions used here: 300 kV accelerating voltage, 0.05 mm Cs, 13.5 mrad convergence angle, 88 mrad inner collection angle. A total of 20 phonon configurations were calculated and a 0.1 nm Gaussian was applied to account for incoherent contributions.

3. Results and Discussion

3.1 Electron Beam-Sample Interactions

The electron beam can be used to reduce CeO_2 and measurements by EELS can observe the subsequent changes to the fine structure of the Ce $\text{M}_{4,5}$ edges (Garvie and Buseck, 1999). In **Figure 1a**, a particle was exposed to two different dose rates. When the dose rate is below a critical threshold, the particle will not reduce within the detection limits, or if it has already been reduced the particle will oxidize. When the particle is exposed to a dose rate above the critical-dose rate threshold the particle reduces as oxygen vacancies are created. This process is repeatable and the damage mechanisms active under these conditions do not significantly disrupt the Ce-sub lattice as the particle morphology does not significantly change after being exposed to the beam (Figure 1b and 1c). While no significant restructuring (e.g., formation of voids,

protrusions, or gross changes in shape) of the particle morphology is perceptible, small changes in facet lengths were measured. Mobility of the surface atoms in CeO₂ nanomaterials under electron irradiation is consistent with previous reports (Bugnet et al., 2017; Möbus et al., 2011). Momentum transferred from the incident electrons to undercoordinated surface atoms likely imparts sufficient energy for surface atoms to diffuse (i.e., knock-on displacement) to more energetically favorable configurations thereby changing the facet sizes.

When the particle is oriented to a zone axis facilitating axial channeling of the electrons (orientations that support planar channeling may also enable this phenomenon but were not tested) additional information about the redox process is present in the ADF-STEM image contrast. Specifically, the image contrast becomes sensitive to regions with point defects (ordered oxygen vacancies would indicate a phase change and could be identified using traditional techniques). This can be understood as atomic static displacements in proximity to oxygen vacancies affecting channeling of the incident electrons along the atomic columns while suppressing coherent scattering. The phenomenon of point defects influencing electron scattering has been covered in-depth elsewhere (Cowley, 1995; Grillo et al., 2008; Hall et al., 1966; Johnston-Peck et al., 2016b; Muller et al., 2004; Perovic et al., 1993; Rossouw et al., 1994). Practically this means under equivalent conditions a HAADF image of CeO_{2-x} (fluorite structure with oxygen vacancies or anion-deficient fluorite) will exhibit lower intensity (image grayscale values) than CeO₂ (fluorite structure without oxygen vacancies) thereby generating contrast. There is a detection limit dependent both on microscope settings and sample conditions and here a single point defect does not alter the electron scattering enough to generate perceptible contrast. Rather the presence of multiple defects per projected atomic column will be necessary to produce contrast.

This described contrast behavior is demonstrated in **Figure 2** as the nanocube is reduced, changes in HAADF contrast with corresponding EELS measurements are shown. The nanocube is oriented to a $\langle 001 \rangle$ zone axis. From the image contrast, we observed the concentration of oxygen vacancies first increases adjacent to exposed surfaces and propagates to the particle core (Frame 251 to Frame 315). Note the nanocube face near the top of the image is in contact with another nanocube inhibiting oxygen desorption so the bottom half of the nanocube reduces more quickly than the top half. This leads to the asymmetric contrast behavior observed in the image series. The Ce white-line ratios increase, indicating reduction, coincident with the image contrast changes. As this process continues, the concentration of oxygen vacancies increases and anion vacancy ordering initiates as identified by the appearance of additional reflections in the fast Fourier transform (Frame 630). This results in the formation of the cubic sesquioxide phase (C-Ce₂O₃, bixbyite structure), first at regions adjacent to the surface and then in the core. The C-Ce₂O₃ assignment was consistent with the indexing results from two additional crystallographic orientations and EELS measurements indicating the oxidation state of the Ce ions were nominally Ce³⁺ (or slightly higher as C-Ce₂O₃ can form over a range of stoichiometries) (Adachi and Imanaka, 1998; Kümmerle and Heger, 1999). During this process the cation sub-lattice does not restructure and remains related (as what amounts to a distorted fcc lattice) to the original fluorite structure as illustrated in the unit cell models of **Figure 3**. From several particles analysis of FFTs comparing the lattice spacings of the $\{200\}_{\text{CeO}_2}$ and $\{400\}_{\text{Ce}_2\text{O}_3}$ reflections measured an average expansion of $\approx 3.4\%$.

After reducing the particle and as the electron dose rate decreases below a critical threshold the particle begins to oxidize, as the cubic sesquioxide (C-Ce₂O₃) phase is energetically unfavorable when compared to CeO₂ (Petit et al., 2005). As oxygen vacancies are annihilated

the anion vacancy ordering in proximity to the nanocube surface is eliminated transitioning from C-Ce₂O₃ to CeO_{2-x}, as further time elapses the core converts to CeO_{2-x}. Next the image grayscale values of the surface regions increase contrasting with the core, indicating that the particle surface has reverted to approximately stoichiometric CeO₂ while the core remains CeO_{2-x}. The contrast between the core and surface eventually resides giving the nanocube a homogenous appearance indicating the entire nanocube has transformed back CeO₂. This process can be repeated many times with approximately the same behavior observed each time. The complete reduction and oxidation process of a CeO₂ nanocube can be viewed in movie “Cube_Redox” in the Supporting Information. The in-situ transformation to the C-Ce₂O₃ phase has been reported previously driven by electron beam reduction (Ding et al., 2016; Haigh et al., 2011; Johnston-Peck et al., 2016a; Sinclair et al., 2017) or a reducing gas environment (Crozier et al., 2008; Wang et al., 2009). We will focus on two parts of the oxidation and reduction process in greater detail, the formation of C-Ce₂O₃ and the oxidation process which occurs after reduction.

3.2 C-Ce₂O₃ Formation

Most recently the structure of C-Ce₂O₃ was refined using single crystal neutron scattering (Kümmerle and Heger, 1999). The unit cell is approximately twice the size of the fluorite structure and belongs to space group $Ia\bar{3}$. Oxygen vacancies align along $\langle 111 \rangle$ directions and result in displacement of adjacent Ce ions away from the vacancies and O ions toward the vacancies. Image simulation of the C-Ce₂O₃ and CeO₂ phases oriented to a $\langle 001 \rangle$ direction is shown in Figure 3. The striped appearance, due to the Ce ions at the 24d sites relaxing away from their original fcc sites, of the C-Ce₂O₃ phase in the simulated data is mimicked in experimental data shown in **Figure 4c**. As vacancies order during the transition between fluorite (CeO_{2-x}) and sesquioxide (C-Ce₂O₃) multiple domains were observed to nucleate. Relative

differences in oxygen vacancy ordering with respect to the parent fluorite lattice create domains which can be related to one another through a translation or rotation, meaning that anti-phase boundaries and orientation variants are present within the particle. An example of a nanocube with different C-Ce₂O₃ domains is shown in Figure 4c. Repeated reduction-oxidation sequences of the same nanocube using the same dose rate did not produce identical C-Ce₂O₃ domain structures, rather the size and orientation of the C-Ce₂O₃ domains was different with each reduction (Supporting Information Figure S1). This suggests that under these conditions the nucleation and growth of C-Ce₂O₃ was not controlled by the applied dose rate, which influences rate of reduction, but other factors.

Oxygen vacancy ordering is a competition between the chemical potential of enthalpy and configurational entropy of oxygen vacancies. The abundance of free surfaces where oxygen vacancies are introduced and the stochastic nature of beam driven reduction creates a situation where fluctuations in vacancy concentrations develop. At critical oxygen vacancy concentrations C-Ce₂O₃ can form and grow. Because the spatial position of these critical concentrations is not controlled here and because C-Ce₂O₃ can only form and grow at critical concentrations, the domain structure does not appear identical with repeated reduction. In situations where the introduction and assembly of vacancies is more precise, the formation of C-Ce₂O₃ domains may show repeatable behavior. This may be achieved when oxygen vacancy injection is spatially controlled (e.g., by limiting the number of free surfaces) or creating a potential for vacancy diffusion through electrical bias. Strain in epitaxial films has been also suggested as a potential mechanism to dictate the domain structure (Sinclair et al., 2017).

3.3 Oxidation Behavior

Background gases in the microscope column oxidize the reduced ceria particles. The composition of background gases in our FEI Titan 80-300 is unknown because gas monitoring equipment (e.g., residual gas analyzer) is not present. In vacuum systems pumped by turbomolecular pumps it is reported that the concentration of molecular oxygen and carbon dioxide is low compared to that of water vapor (Postek, 1996). Data from a residual gas analyzer (RGA) attached to the ESTEM corroborates this result (Supporting Information Figure S2). Therefore, the oxidation process is assumed to be dominated by the absorption and dissociation of water vapor because water vapor will interact with nanoparticle surface at the highest frequency of all oxidizing species present, although molecular oxygen will also contribute.

As the nanocube oxidizes the phase transitions from C-Ce₂O₃ to CeO_{2-x} to CeO₂. The transitions initiate near surfaces and the core follows. In **Figure 5** images from a nanocube oxidizing after being reduced by the electron beam are shown. At this point in the process CeO_{2-x} is present and the C-Ce₂O₃ phase is no longer detected. As time proceeds, the image intensity initially increases in the regions adjacent to the corners (Figure 5b and 5c) – which are terminated by {111} and {110} facets – reflecting further oxidation to CeO₂. This intensity increase is then observed in regions adjacent to faces (Figure 5d and 5e) – which are terminated by {100} facets – and then within the particle core (Figure 5f). A model and micrographs depicting the nanocube geometry and surface terminations are shown in Supporting Information Figure S3. To highlight these contrast changes, the difference in image intensity between the first image (Figure 5a) and each following image (Figure 5b-5f) is shown below each respective image. To do this the images were aligned using a rigid registration routine implemented in FIJI (Schindelin et al., 2012; Schneider et al., 2012; Thevenaz et al., 1998). To improve signal to noise and minimize the effect of non-linear distortions which are not corrected by rigid

registration, the average intensity of three images (the image shown along with the preceding and following images of the time series) is calculated. This contrast behavior was similarly observed in subsequent redox cycles on the same nanocube (Supporting Information Figures S4 and S5) as well as in other nanocubes (Supporting Information Figures S6 and S7) suggesting this behavior is characteristic to nanocubes under these conditions.

This experiment was repeated on truncated octahedra and an example of reduction and oxidation can be viewed in movie “TruncatedOctahedron_Redox” in the Supporting Information. The truncated octahedra were oriented to $\langle 110 \rangle$ zone axes and further information on particle geometry and surface terminations are shown in Supporting Information Figure S8. In **Figure 6** images from a truncated octahedron oxidizing from CeO_{2-x} to CeO_2 are shown. As time proceeds, the image intensity initially increases in the regions adjacent to the particle tips (Figure 6b and 6c) – which are terminated $\{100\}$ facets – to regions adjacent to faces (Figure 6d and 6e) – which are terminated by $\{111\}$ facets – and then the particle the core (Figure 6f). This contrast behavior was also reproducible (Supporting Information Figures S9 and S10).

In these image series because the image contrast reflects regions with different concentrations of oxygen vacancies, this means that regions adjacent to corners and tips are oxidizing more quickly than regions adjacent to faces. In nanocubes the corners are bound by $\{111\}$ and $\{110\}$ facets while in truncated octahedra the tips are bound by $\{100\}$ facets. It can be hypothesized the cause of this observed behavior is influenced by geometric and facet effects. Near corners and tips of the nanocubes and truncated octahedra the portion of atoms at the surface increases per atomic column (Supporting Information Figure S11). As such, diffusion path lengths from the surface to oxygen vacancies in the bulk would be comparatively shorter in these regions and presumably would oxidize more quickly. Alternatively, differences between

facets in the process of gas adsorption and subsequent absorption of oxygen into the lattice could also influence the oxidation process. On ceria water vapor adsorbs dissociatively as -OH and -H groups and these groups can either recombine and desorb as water or the hydroxyl group can cleave leading to the formation and desorption of molecular hydrogen.(Molinari et al., 2012) The latter will oxidize the reduced ceria while the former leaves the oxidation state unchanged. Differences in the thermodynamics or kinetics of this process as a function of surface termination would subsequently influence the rate of oxidation.

To deconvolute the geometric effect from the facet behavior, simulations and kinetic data comparing the behavior of cubes and truncated octahedra were used. In nanocubes the surface is predominately {100} terminated while in truncated octahedra the surfaces are predominately {111} terminated. {110} surfaces are present on the nanocubes but not the truncated octahedron so their contribution will be ignored from this point in the discussion. Therefore, if the relative activity of {111} and {100} surfaces differs, this will manifest as differences in the rate of oxidation displayed by nanocubes and truncated octahedra. Diffusion modeled by the finite element method (FEM) was compared to the spatially dependent oxidation behavior observed in HAADF-STEM (Figures S12 and S13). While kinetic data, comparing EELS oxidation state values as a function of time controlling for environment and electron beam exposure conditions, was analyzed to look for differences in redox rates as a function of particle geometry (Figures S14 and S15). Details on both these analyses are in the Supporting Information. The FEM diffusion models indicate that in nanocubes {100} surfaces alone do not account for the oxidation activity observed in HAADF images. While EELS data indicates that under for a given set of electron beam conditions nanocubes will reduce to a greater extent and at a faster rate than truncated octahedra. Also, truncated octahedra oxidize at a faster rate than nanocubes.

This indicates that for these conditions {111} facets are more stable and have higher activity for the oxidation process.

These results of facet dependent behavior agree with prior DFT calculations. Molinari *et al.* indicated the heat of reduction for the {111} and {100} surfaces are 2.01 eV and 1.61 eV, respectively (Molinari et al., 2012). Surface studies comparing epitaxial thin films with {111} and {100} termination have reached mixed conclusions (Henderson et al., 2003; Mullins et al., 2012). Mullins *et al.* compared reduced {111} and {100} surfaces and demonstrated that reduced {111} surfaces tend to decompose adsorbed hydroxyls and form hydrogen thereby oxidizing while {100} surfaces promote water formation and no change of state. (Mullins et al., 2012) While Henderson *et al.* reports {111} surfaces are less favorable than non-{111} surfaces for oxidation by water (Henderson et al., 2003). Mullins *et al.* suggested differences originating in sample preparation and defect populations as a possible explanation for this discrepancy (Mullins et al., 2012). Using the methods presented here, STEM affords the possibility to directly relate specific structures with performance offering a potential route to elucidate the origin of such competing observations.

3.4 ESTEM Measurements

The oxidation of reduced ceria nanoparticles in the high vacuum environment of the microscope suggests that the particles have a low energy, equilibrium state that is kinetically accessible on the time scale of our experimental observations. Accordingly, to better understand how the environment of the analytical tool can influence the outcome of measurements we used ESTEM to understand how oxygen partial pressure influences the threshold for beam reduction and the oxidation state of the particle.

To investigate the role of atmosphere on the critical dose rate threshold a nanocube was exposed to different dose rates and pressures of oxygen. Under vacuum conditions the oxidation state of the cerium atoms was recorded as a function of cumulative dose for three different dose rates. Below the critical-dose rate threshold, no detectable change in oxidation state was observed. While above the critical dose rate, the particle was reduced (Supporting Information Figure S16) in accordance with prior results (Johnston-Peck et al., 2016a). The same experiment was then repeated with molecular oxygen introduced to the sample environment. Results in **Figure 7** demonstrate the increase in oxygen pressure increased the critical dose rate threshold. A similar observation was recently made on CeO₂ films using TEM (Sinclair et al., 2017). This observation can be understood as the rate balance between the electron beam driven reduction process and the tendency of CeO_{2-x} to oxidize. As the pressure of molecular oxygen increases the frequency of collisions between the ceria particle and the oxidizing species increases. This increases the rate at which oxygen can adsorb and subsequently annihilate any oxygen vacancies that were created by electron beam-specimen interactions. Therefore, for a fixed dose rate, when the pressure of oxidizing species is low, vacancies are created at a rate faster than they are annihilated, the vacancies accumulate, and EELS can detect reduction of the cerium atoms. When the pressure increases, the vacancies are annihilated at the same approximate rate at which they are generated such that vacancies do not accumulate and EELS does not detect reduction of the cerium atoms.

In electron microscopy studies it is commonly reported that the surface of CeO₂ nanoparticles are reduced. This observation has been made with direct measurements using STEM-EELS and imaging techniques (Goris et al., 2014; Haigh et al., 2011; Johnston-Peck et al., 2016b; Lin et al., 2014; Spadaro et al., 2016; Turner et al., 2011; Wu et al., 2004), and can be

inferred by observing the Ce^{3+} concentration in ceria particles is inversely related to diameter (Sims et al., 2018; Spadaro et al., 2016; Wu et al., 2004). To determine if the microscope environment influences the oxidation state of CeO_2 particles the oxygen chemical potential of the ESTEM was changed. Particles ≈ 5 nm in diameter, as shown in **Figure 8a**, were studied. The small size of the particles means the surface area to volume ratio is higher than the nanocubes and truncated octahedra and any surface effects will be greater. EEL spectra were recorded in vacuum and under two different pressures of oxygen. Representative spectra recorded from ensembles of particles under each condition are shown in Figure 8b and quantification of the Ce $\text{M}_{4,5}$ edge into Ce^{3+} and Ce^{4+} content is shown in Table 1. As the pressure of oxygen increases, the Ce^{3+} content decreases from 11.4% when measured in vacuum to 0.4% when measured with a pressure of ≈ 158 Pa oxygen.

To mitigate the reducing effect of the electron beam both dose rate and total dose were minimized by setting the beam current to ≈ 10 pA and recording both the individual core loss and low loss spectrum over a period of 1.1 s. Further, single particle studies were avoided and the electron beam was scanned over an area of 729 nm^2 during the spectral acquisition, so each spectrum reflects the oxidation state of many particles averaged. Control experiments in vacuum indicate that no additional reduction was observed using these conditions for exposures lasting longer than 1.1s. This demonstrates that the microscope environment influences the Ce^{3+} content, specifically the vacuum environment increases the Ce^{3+} content relevant to its state in environments with greater oxygen pressures. While the reduction of bulk CeO_2 is reported to occur at either lower pressures or higher temperatures than those used here (Bevan and Kordis, 1964; Ricken et al., 1984) this difference in behavior can be understood as the manifestations of the size of the particles and the gaseous environment. Both experimental studies and

calculations indicate surface regions are more susceptible than bulk to reduction (Botu et al., 2014; Kim et al., 2004; Nolan et al., 2006). This is further exacerbated in redox (containing both reducing and oxidizing gases) environments (Botu et al., 2014), as is created by the background gases of the ESTEM (Supporting Information Figure S2). While these EELS measurements were not spatially resolved and therefore did not discriminate between the particle surface and core during acquisition presumably a majority of the Ce^{3+} atoms are located near the particle surface in accordance with the aforementioned findings (Goris et al., 2014; Haigh et al., 2011; Johnston-Peck et al., 2016b; Lin et al., 2014; Spadaro et al., 2016; Turner et al., 2011; Wu et al., 2004). Therefore, as oxygen is introduced, the oxygen chemical potential increases, stabilizing stoichiometric CeO_2 at the surface and reducing the Ce^{3+} content. Because the ≈ 5 nm particles studied have a large surface to volume ratio this behavior becomes pronounced even though the measurements were spatially averaged. Whereas spatially-averaged EELS measurements from large particles would be less sensitive to the surface region and this effect over the range of pressures considered here would presumably be negligible, as large particles have been shown to have only a few percent Ce^{3+} content as measured in STEM under vacuum conditions (Sims et al., 2018; Wu et al., 2004).

Because particle size and surface effects are often of interest, it is important to contextualize results to separate contributions due to the extrinsic, environmental factors from those that may be due to intrinsic effects. This is important when comparing and interpreting results that have been recorded from different instruments with different environments. As well as when addressing fundamental questions, such as, whether the lattice expansion inversely proportional to particle diameter observed in TEM measurements (Hailstone et al., 2009; Tsunekawa et al., 1999; Wu et al., 2004) is the result of the measurements being taken in a

reducing environment (where lattice parameter dilates due phenomenon associated with reduction of Ce^{4+} to Ce^{3+}) or others factors such as capillary pressure caused by surface stress (Diehm et al., 2012). Or how aliovalent dopants atoms spatially localize and influence the oxygen vacancy concentrations relative to bulk and surface (Collins et al., 2017). While the measurements here indicate that environment can influence the outcome of certain results, comprehensive measurements will be needed to address the aforementioned questions and quantitatively establish the *spatial* concentration of Ce^{3+} atoms in particles as a function of atmosphere, potentially extracting thermodynamic information.

Without the ability to accurately measure the makeup of the microscope environment certain data interpretation and comparison is hindered. As discussed by Miller and Crozier (Miller and Crozier, 2014), EELS and RGA have limitations when quantifying gas species. EELS lacks sensitivity at low pressures and limits what other measurements can be made simultaneously. RGAs may operate at different pressures than the sample environment and may not be attached in the direct vicinity of the sample. As a result, differences in gas diffusivities can skew quantification. Further, RGA measures the mass/charge ratio and that also poses challenges to accurate identification and quantification. Water vapor and oxygen sensors mounted in the immediate vicinity of the sample should be able to address some of these limitations and be of value for studies when knowing the environmental characteristics is critically important.

4. Conclusions

The methodology we have presented demonstrates the possibility of a single particle technique to provide insight on structural-property relationships. These techniques are useful

because they can complement global measurements or first-principal calculations, which may not capture the complexity and variable nature of a dynamic system and its microstructure.

Specifically, we have demonstrated that CeO₂ truncated octahedra terminated predominately with {111} surfaces compared to nanocubes terminated predominately with {100} surfaces are more resistant to reduction and once reduced will oxidize more quickly. These redox experiments were conducted in vacuum at room temperature using the electron beam to stimulate the reduction process. It is unknown if this reduction pathway is practically equivalent to that of a gaseous reducing environment and establishing equivalence between the two different reduction processes will be important if beam-mediated reduction is to be used as a stimulus for applied studies.

Conducting measurements like these under controlled temperature and gas environments may be able to provide additional insight into the catalytic behavior of CeO₂ as a function of structural parameters. Moreover, the HAADF-STEM image contrast mechanism responsible for the sensitivity to the anion-deficient fluorite phase is not necessarily limited to applications in the Ce-O system or even oxides. Point defects that locally distort the surrounding crystal lattice will alter the electron scattering behavior and potentially generate image contrast. This means that it may also be possible to use these techniques to monitor other reactions such as intercalation. However, it is prudent to use independent verification, either through calculations or other measurement techniques, to verify that the physical change in the structure is associated with the observed contrast change.

ESTEM measurements link oxygen chemical potential of the microscope environment and the results of oxidation state measurements in ceria particles. Under certain conditions instrumental influence may become an important consideration for comparing results acquired

from different platforms, as well as attempting to interpret functional properties and establish structure-property relationships. This highlights the importance of tools and techniques that accurately quantify the composition of the instrument environment.

Acknowledgements

We thank Christopher M. Sims and Russell A. Maier (National Institute of Standards and Technology) for providing the CeO_2 and CeAlO_3 powders. We thank W. David Wei, Joseph D. Duchene, and Alan D. Roberts (University of Florida) for providing the CeO_2 nanocubes. W.-C.D. Yang acknowledges support under the Cooperative Research Agreement between the University of Maryland and the National Institute of Standards and Technology Center for Nanoscale Science and Technology, award 70NANB10H193, through the University of Maryland.

Disclaimer: Certain commercial equipment, instruments, or materials are identified in this paper in order to specify the experimental procedure adequately. Such identification is not intended to imply recommendation or endorsement by the National Institute of Standards and Technology, nor is it intended to imply that the materials or equipment identified are necessarily the best available for the purpose.

Figures

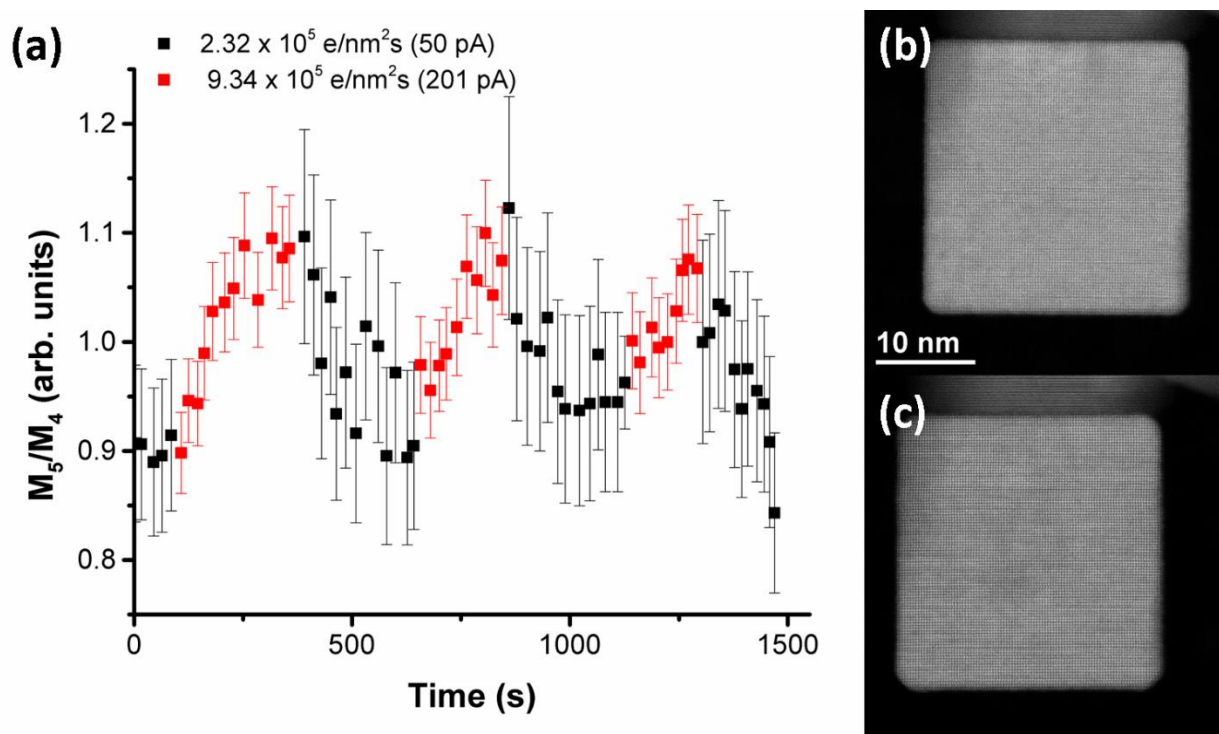


Figure 1. The ratio of the Ce $M_{4,5}$ peaks as a function of time as the dose rate was changed. Increases in the M_5/M_4 ratio reflect an increased Ce^{3+} concentration. When the dose rate is above the critical-dose rate threshold (red points) the particle reduces, conversely when the dose rate is below the critical-dose rate threshold (black points) the particle oxidizes. HAADF-STEM images of the particle before (b) and after (c) the exposure experiment in (a).

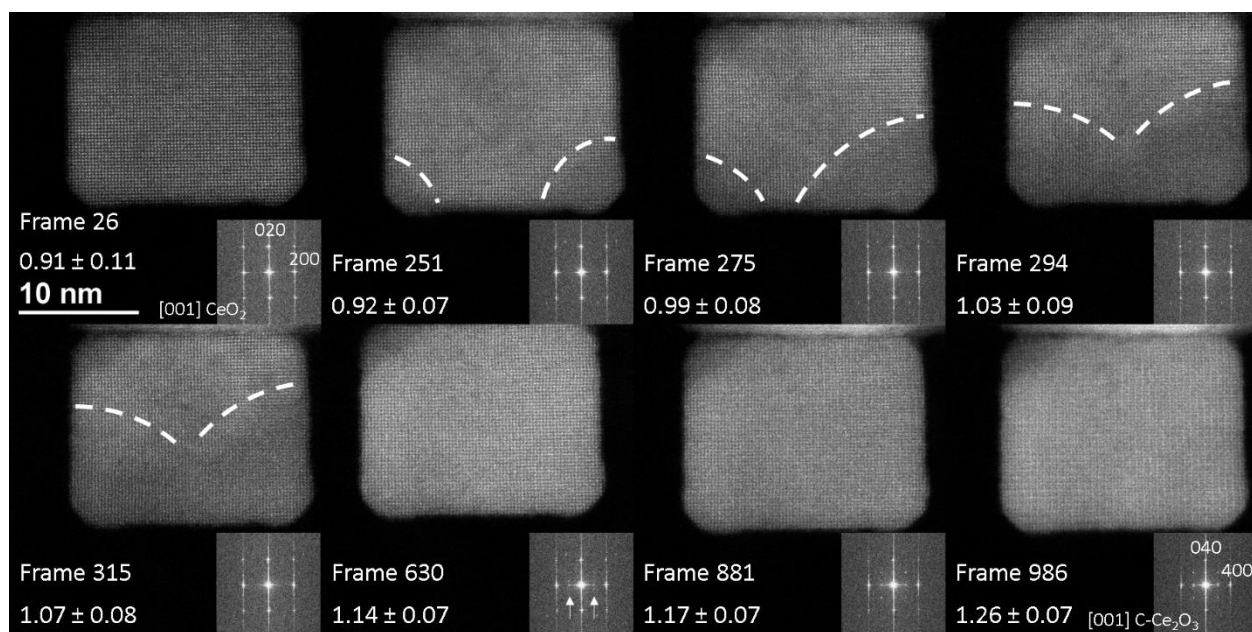


Figure 2. A series of HAADF-STEM images with FFT of a CeO₂ nanocube being reduced to C-Ce₂O₃. As CeO_{2-x} forms contrasting regions can be observed in Frames 251, 275, 294, and 315 and are marked with dashed lines. In Frame 630 the onset of oxygen vacancy ordering is observed and C-Ce₂O₃ begins forming, arrows in the FFT indicate the presence of new reflections associated with the phase change to C-Ce₂O₃. Ce M_{4,5} white-line ratio EELS measurements reported in the bottom left-hand corner, correlate the change in image contrast to a change in cerium oxidation state. Dose rates: Frame 26 – $3.24 \times 10^5 \text{ e} \cdot \text{nm}^{-2} \cdot \text{s}^{-1}$; Frame 251, 275, 294, 315 – $5.56 \times 10^5 \text{ e} \cdot \text{nm}^{-2} \cdot \text{s}^{-1}$; Frame 630 – $9.26 \times 10^5 \text{ e} \cdot \text{nm}^{-2} \cdot \text{s}^{-1}$; Frame 881, 986 – $1.11 \times 10^6 \text{ e} \cdot \text{nm}^{-2} \cdot \text{s}^{-1}$. The vertical streaking in the FFTs is due to scan noise.

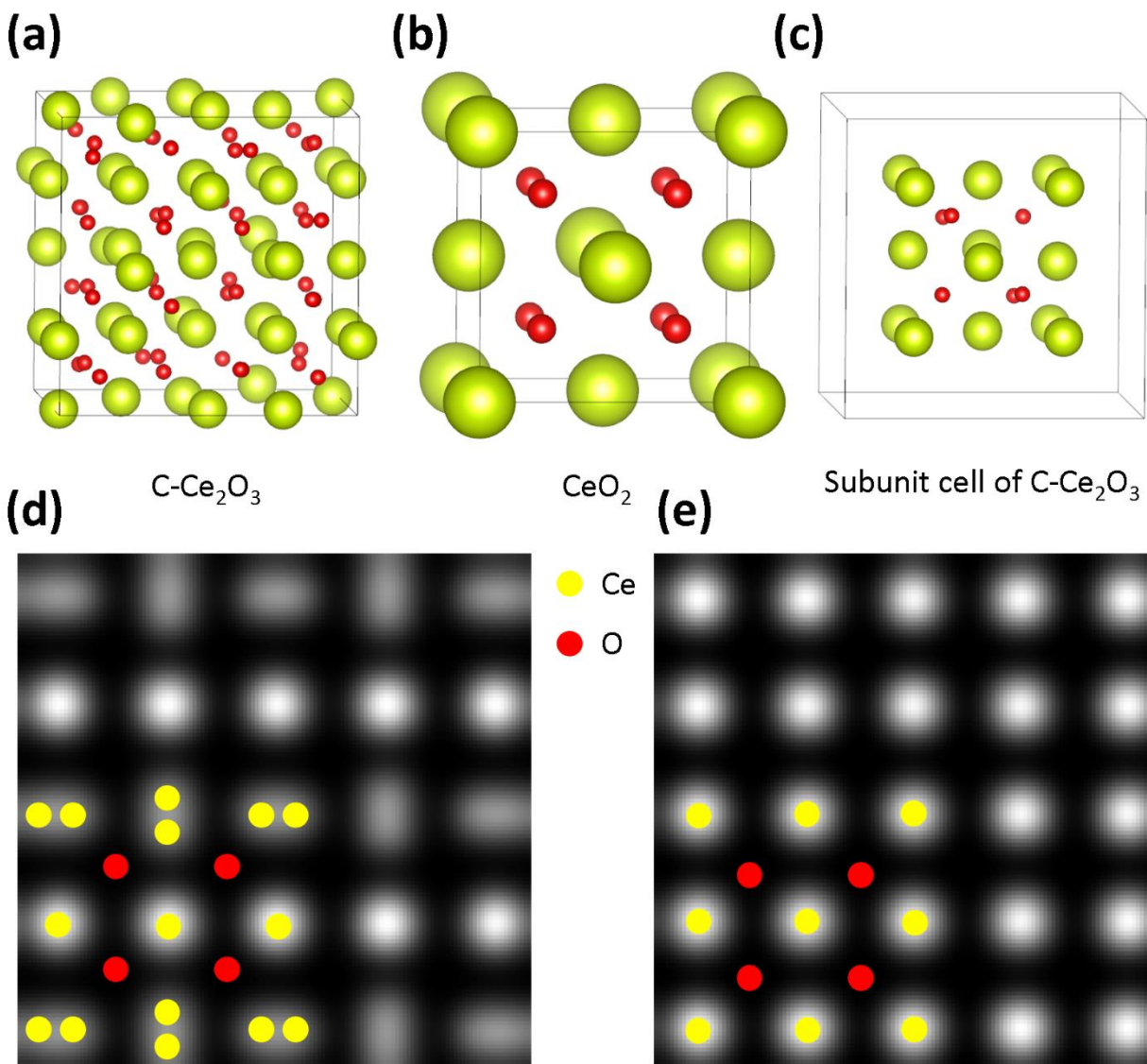


Figure 3. Unit cell models of C-Ce₂O₃ (a) and CeO₂ (b). Isolating a portion of the C-Ce₂O₃ unit cell highlights the similarities between the two phases (c). Simulated HAADF images of C-Ce₂O₃ (d) and CeO₂ (e) oriented to a <001> zone axis. The yellow and red markers indicate the position of Ce and O atomic columns, respectively.

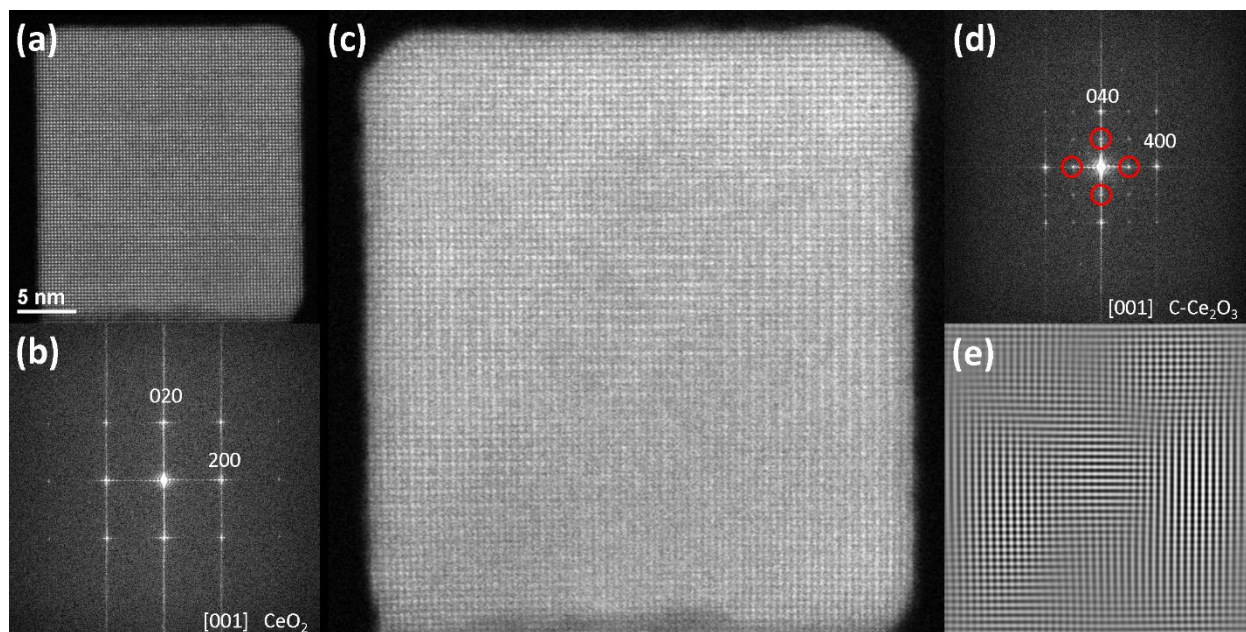


Figure 4. HAADF-STEM image of a fluorite CeO_2 cube (a) taken at a dose rate of $2.74 \times 10^5 \text{ e} \cdot \text{nm}^{-2} \cdot \text{s}^{-1}$ (probe current of $\approx 30 \text{ pA}$). The FFT of the image is shown in (b). The same particle exposed to a higher dose rate of $1.82 \times 10^6 \text{ e} \cdot \text{nm}^{-2} \cdot \text{s}^{-1}$ (probe current of $\approx 200 \text{ pA}$) transforms into sesquioxide $\text{C-Ce}_2\text{O}_3$ (c). The FFT of the image is shown in (d) contains reflections not observed in (b). The $\text{C-Ce}_2\text{O}_3$ {200} and {020} reflections marked by red circles in (d) are masked and an inverse FFT is calculated (e) highlighting the $\text{C-Ce}_2\text{O}_3$ domain structure.

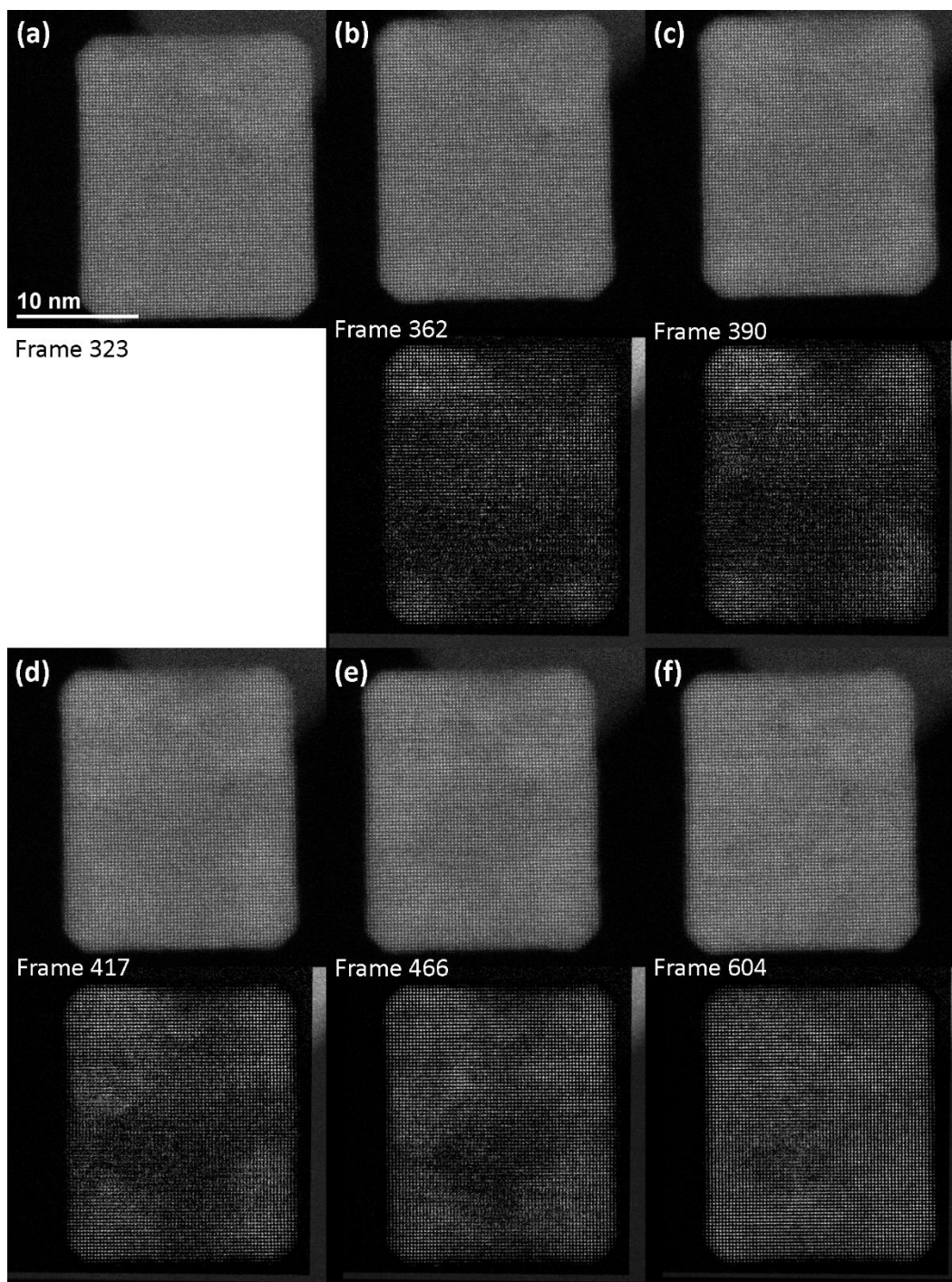


Figure 5. Time series of a CeO_2 nanocube oxidizing from CeO_{2-x} to CeO_2 . Select frames are shown. The increase in intensity from (a) is shown (b-f) below the original image. Contrast changes appear first at corners. Dose rate: $3.70 \times 10^5 \text{ e} \cdot \text{nm}^{-2} \cdot \text{s}^{-1}$

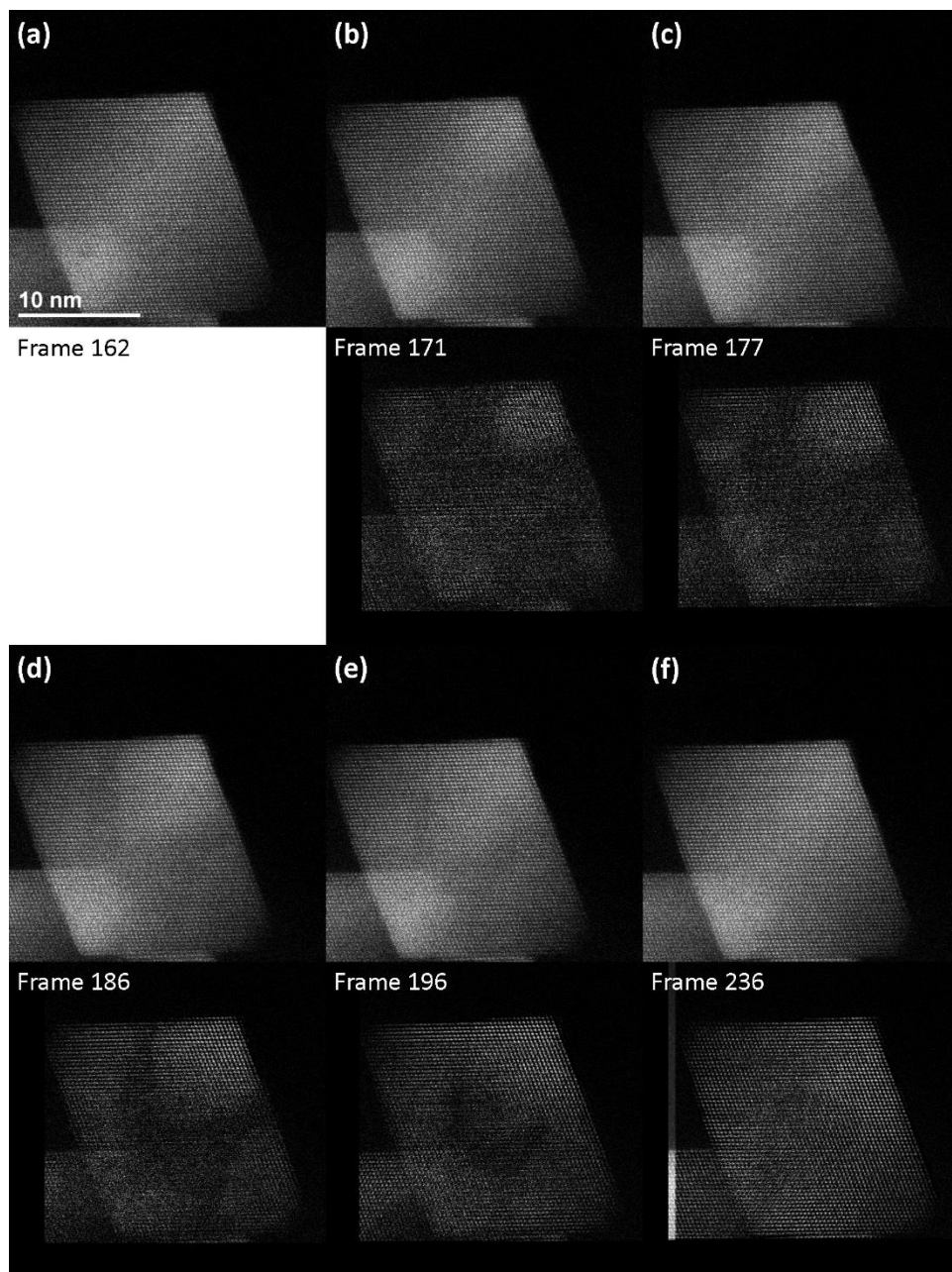


Figure 6. Time series of a CeO_2 truncated octahedron oxidizing from CeO_{2-x} to CeO_2 . Select frames are shown. The increase in intensity from (a) is shown (b-f) below the original image. Contrast changes appear first at tips. Dose rate: $4.54 \cdot 10^5 \text{ e}^- \cdot \text{nm}^{-2} \cdot \text{s}^{-1}$

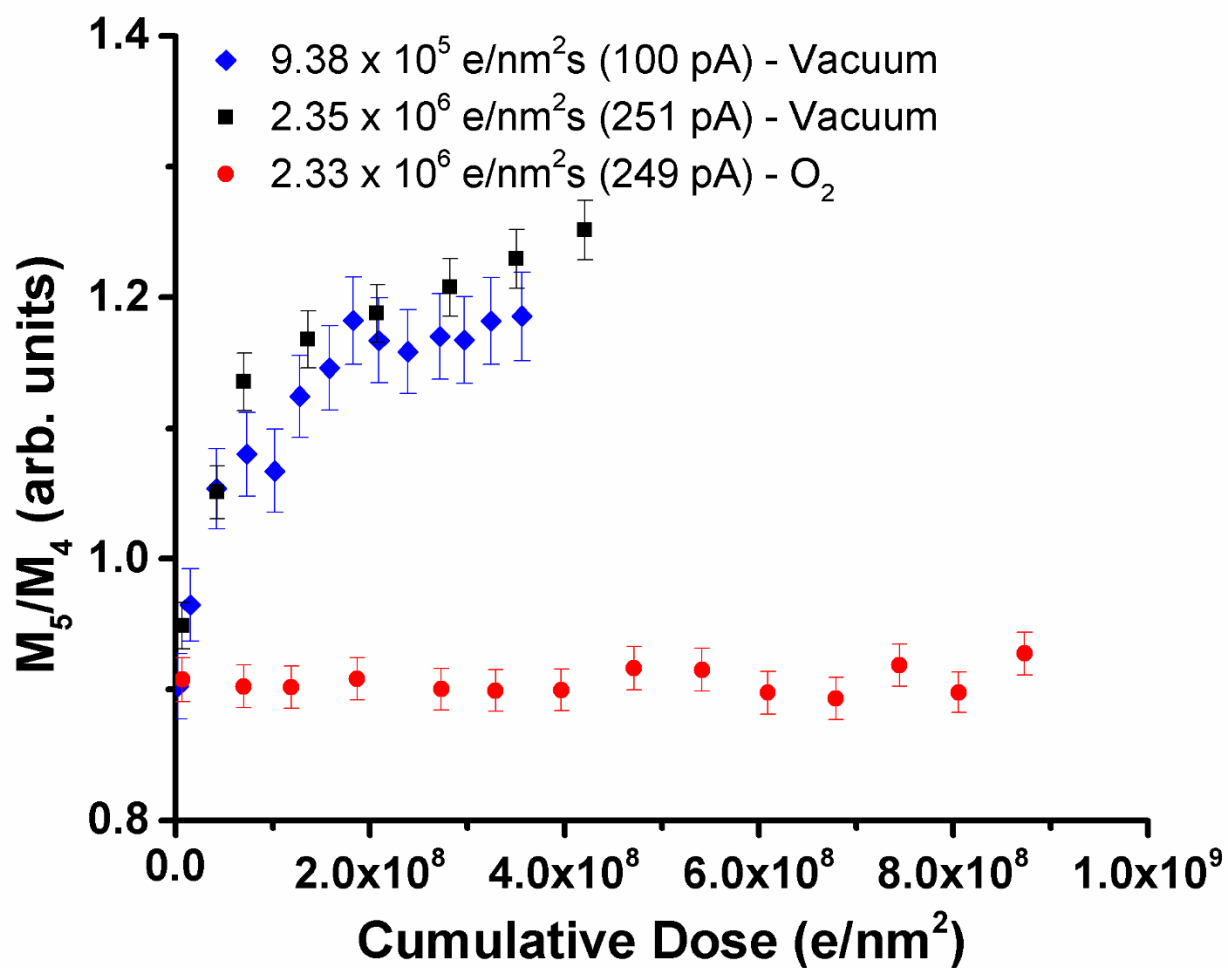


Figure 7. White-line ratio of the Ce $M_{4,5}$ edge from a CeO_2 nanocube as a function of cumulative dose. Under vacuum the nanocube reduces. When oxygen is introduced raising the system pressure by over an order of magnitude, no detectable reduction occurs.

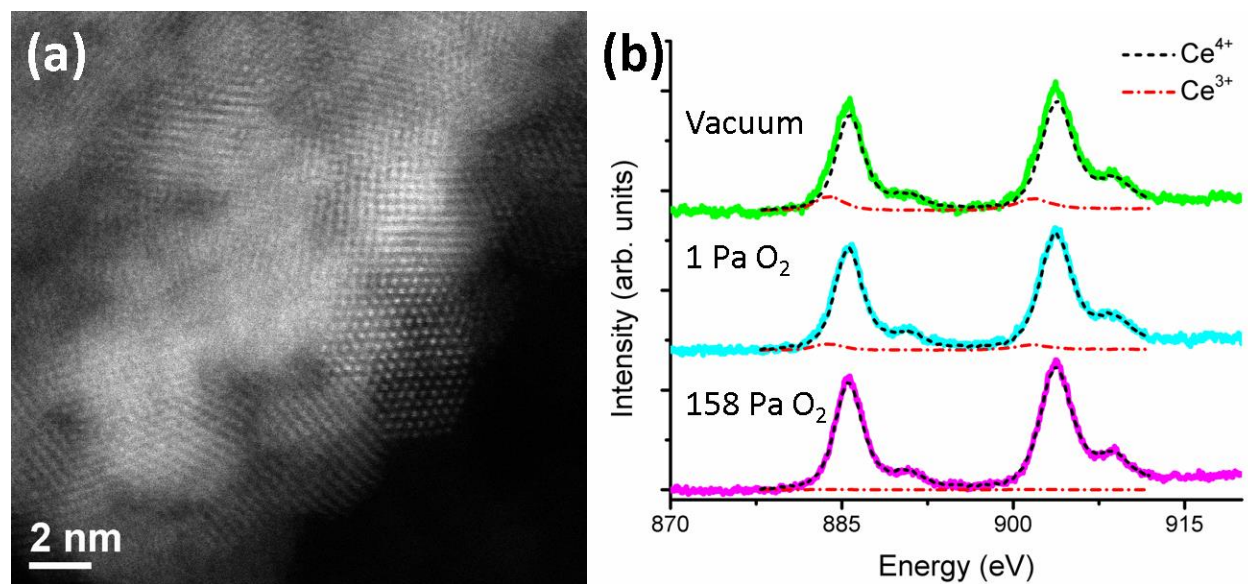


Figure 8. A representative HAADF-STEM image of the CeO₂ particles. Representative EEL spectra of the Ce M_{4,5} edge for each gas condition. The fitted weight of Ce³⁺ and Ce⁴⁺ reference spectra are shown in red and blue underneath each spectrum.

Table 1. Oxidation state of the ceria powder under different atmospheres

Gas	Pressure (Pa)	% Ce ³⁺	σ
Oxygen	≈ 158	0.4	0.8
Oxygen	≈ 1	4.4	2.3
Vacuum	$\approx 2 \cdot 10^{-5}$	11.9	2.5

References

- Adachi, G., Imanaka, N., 1998. The binary rare earth oxides. *Chemical Reviews* 98, 1479-1514.
- Bevan, D.J.M., Kordis, J., 1964. Mixed oxides of the type MO_2 (fluorite)— M_2O_3 —I oxygen dissociation pressures and phase relationships in the system $\text{CeO}_2 \cdot \text{Ce}_2\text{O}_3$ at high temperatures. *Journal of Inorganic and Nuclear Chemistry* 26, 1509-1523.
- Botu, V., Ramprasad, R., Mhadeshwar, A.B., 2014. Ceria in an oxygen environment: Surface phase equilibria and its descriptors. *Surface Science* 619, 49-58.
- Bugnet, M., Overbury, S.H., Wu, Z.L., Epicier, T., 2017. Direct visualization and control of atomic mobility at {100} surfaces of ceria in the environmental transmission electron microscope. *Nano Letters* 17, 7652-7658.
- Collins, S.M., Fernandez-Garcia, S., Calvino, J.J., Midgley, P.A., 2017. Sub-nanometer surface chemistry and orbital hybridization in lanthanum-doped ceria nano-catalysts revealed by 3D electron microscopy. *Scientific Reports* 7, 5406.
- Cowley, J.M., 1995. *Diffraction Physics*, Third ed. Elsevier, Amsterdam.
- Crozier, P.A., Wang, R., Sharma, R., 2008. In situ environmental TEM studies of dynamic changes in cerium-based oxides nanoparticles during redox processes. *Ultramicroscopy* 108, 1432-1440.
- Diehm, P.M., Ágoston, P., Albe, K., 2012. Size-dependent lattice expansion in nanoparticles: Reality or anomaly? *ChemPhysChem* 13, 2443-2454.
- Ding, Y., Chen, Y., Pradel, K.C., Liu, M., Wang, Z.L., 2016. In-situ transmission electron microscopy study of oxygen vacancy ordering and dislocation annihilation in undoped and Sm-doped CeO_2 ceramics during redox processes. *Journal of Applied Physics* 120, 214302.
- Garvie, L.A.J., Buseck, P.R., 1999. Determination of $\text{Ce}^{4+}/\text{Ce}^{3+}$ in electron-beam-damaged CeO_2 by electron energy-loss spectroscopy. *Journal of Physics and Chemistry of Solids* 60, 1943-1947.
- Goris, B., Turner, S., Bals, S., Van Tendeloo, G., 2014. Three-dimensional valency mapping in ceria nanocrystals. *ACS Nano* 8, 10878-10884.
- Grillo, V., Carlino, E., Glas, F., 2008. Influence of the static atomic displacement on atomic resolution Z-contrast imaging. *Physical Review B* 77, 054103.
- Haigh, S.J., Young, N.P., Sawada, H., Takayanagi, K., Kirkland, A.I., 2011. Imaging the active surfaces of cerium dioxide nanoparticles. *ChemPhysChem* 12, 2397-2399.
- Hailstone, R.K., DiFrancesco, A.G., Leong, J.G., Allston, T.D., Reed, K.J., 2009. A study of lattice expansion in CeO_2 nanoparticles by transmission electron microscopy. *The Journal of Physical Chemistry C* 113, 15155-15159.
- Hall, C.R., Hirsch, P.B., Booker, G.R., 1966. The effect of point defects on absorption of high energy electrons passing through crystals. *Philosophical Magazine* 14, 979-989.
- Henderson, M.A., Perkins, C.L., Engelhard, M.H., Thevuthasan, S., Peden, C.H.F., 2003. Redox properties of water on the oxidized and reduced surfaces of $\text{CeO}_2(111)$. *Surface Science* 526, 1-18.
- Johnston-Peck, A.C., DuChene, J.S., Roberts, A.D., Wei, W.D., Herzing, A.A., 2016a. Dose-rate-dependent damage of cerium dioxide in the scanning transmission electron microscope. *Ultramicroscopy* 170, 1-9.
- Johnston-Peck, A.C., Winterstein, J.P., Roberts, A.D., DuChene, J.S., Qian, K., Sweeny, B.C., Wei, W.D., Sharma, R., Stach, E.A., Herzing, A.A., 2016b. Oxidation-state sensitive imaging of cerium dioxide by atomic-resolution low-angle annular dark field scanning transmission electron microscopy. *Ultramicroscopy* 162, 52-60.
- Kim, S., Merkle, R., Maier, J., 2004. Oxygen nonstoichiometry of nanosized ceria powder. *Surface Science* 549, 196-202.
- Koch, C., 2002. Determination of core structure periodicity and point defect density along dislocations. Arizona State University.

Kümmerle, E.A., Heger, G., 1999. The structures of $\text{C-Ce}_2\text{O}_{3+6}$, Ce_7O_{12} , and $\text{Ce}_{11}\text{O}_{20}$. *J. Solid State Chem.* 147, 485-500.

Lin, Y., Wu, Z., Wen, J., Poeppelmeier, K.R., Marks, L.D., 2014. Imaging the atomic surface structures of CeO_2 nanoparticles. *Nano Letters* 14, 191-196.

Miller, B.K., Crozier, P.A., 2014. Analysis of catalytic gas products using electron energy-loss spectroscopy and residual gas analysis for operando transmission electron microscopy. *Microscopy and Microanalysis* 20, 815-824.

Mitchell, D.R.G., Schaffer, B., 2005. Scripting-customised microscopy tools for Digital Micrograph™. *Ultramicroscopy* 103, 319-332.

Möbus, G., Saghi, Z., Sayle, D.C., Bhatta, U.M., Stringfellow, A., Sayle, T.X.T., 2011. Dynamics of polar surfaces on ceria nanoparticles observed in situ with single-atom resolution. *Advanced Functional Materials* 21, 1971-1976.

Molinari, M., Parker, S.C., Sayle, D.C., Islam, M.S., 2012. Water adsorption and its effect on the stability of low index stoichiometric and reduced surfaces of ceria. *The Journal of Physical Chemistry C* 116, 7073-7082.

Muller, D.A., Nakagawa, N., Ohtomo, A., Grazul, J.L., Hwang, H.Y., 2004. Atomic-scale imaging of nanoengineered oxygen vacancy profiles in SrTiO_3 . *Nature* 430, 657-661.

Mullins, D.R., Albrecht, P.M., Chen, T.-L., Calaza, F.C., Biegalski, M.D., Christen, H.M., Overbury, S.H., 2012. Water dissociation on $\text{CeO}_2(100)$ and $\text{CeO}_2(111)$ thin films. *The Journal of Physical Chemistry C* 116, 19419-19428.

Nolan, M., Fearon, J.E., Watson, G.W., 2006. Oxygen vacancy formation and migration in ceria. *Solid State Ion.* 177, 3069-3074.

Perovic, D.D., Rossouw, C.J., Howie, A., 1993. Imaging elastic strains in high-angle annular dark field scanning transmission electron microscopy. *Ultramicroscopy* 52, 353-359.

Petit, L., Svane, A., Szotek, Z., Temmerman, W.M., 2005. First-principles study of rare-earth oxides. *Physical Review B* 72, 205118.

Postek, M.T., 1996. An approach to the reduction of hydrocarbon contamination in the scanning electron microscope. *Scanning* 18, 269-274.

Ricken, M., Nölting, J., Riess, I., 1984. Specific heat and phase diagram of nonstoichiometric ceria (CeO_{2-x}). *J. Solid State Chem.* 54, 89-99.

Rossouw, C.J., Spellward, P., Perovic, D.D., Cherns, D., 1994. Dynamical zone-axis electron diffraction contrast of boron-doped Si multilayers. *Philosophical Magazine A* 69, 255-265.

Schindelin, J., Arganda-Carreras, I., Frise, E., Kaynig, V., Longair, M., Pietzsch, T., Preibisch, S., Rueden, C., Saalfeld, S., Schmid, B., Tinevez, J.-Y., White, D.J., Hartenstein, V., Eliceiri, K., Tomancak, P., Cardona, A., 2012. Fiji: an open-source platform for biological-image analysis. *Nat Meth* 9, 676-682.

Schneider, C.A., Rasband, W.S., Eliceiri, K.W., 2012. NIH Image to ImageJ: 25 years of image analysis. *Nat Meth* 9, 671-675.

Sims, C.M., Maier, R.A., Johnston-Peck, A.C., Gorham, J.M., Hackley, V.A., Nelson, B.C., 2018. Approaches for the quantitative analysis of oxidation state in cerium oxide nanomaterials. Submitted.

Sinclair, R., Lee, S.C., Shi, Y., Chueh, W.C., 2017. Structure and chemistry of epitaxial ceria thin films on yttria-stabilized zirconia substrates, studied by high resolution electron microscopy. *Ultramicroscopy* 176, 200-211.

Spadaro, M.C., Luches, P., Bertoni, G., Grillo, V., Turner, S., Tendeloo, G.V., Valeri, S., D'Addato, S., 2016. Influence of defect distribution on the reducibility of CeO_{2-x} nanoparticles. *Nanotechnology* 27, 425705.

Thevenaz, P., Ruttimann, U.E., Unser, M., 1998. A pyramid approach to subpixel registration based on intensity. *IEEE Transactions on Image Processing* 7, 27-41.

Tsunekawa, S., Sivamohan, R., Ito, S., Kasuya, A., Fukuda, T., 1999. Structural study on monosize CeO_{2-x} nano-particles. *Nanostructured Materials* 11, 141-147.

Turner, S., Lazar, S., Freitag, B., Egoavil, R., Verbeeck, J., Put, S., Strauven, Y., Van Tendeloo, G., 2011. High resolution mapping of surface reduction in ceria nanoparticles. *Nanoscale* 3, 3385-3390.

Verbeeck, J., Van Aert, S., 2004. Model based quantification of EELS spectra. *Ultramicroscopy* 101, 207-224.

Wang, R., Crozier, P.A., Sharma, R., 2009. Structural transformation in ceria nanoparticles during redox processes. *The Journal of Physical Chemistry C* 113, 5700-5704.

Wu, L., Wiesmann, H.J., Moodenbaugh, A.R., Klie, R.F., Zhu, Y., Welch, D.O., Suenaga, M., 2004. Oxidation state and lattice expansion of CeO_{2-x} nanoparticles as a function of particle size. *Physical Review B* 69, 125415.

Supporting Information

In Situ Oxidation and Reduction of Cerium Dioxide Nanoparticles Studied by Scanning Transmission Electron Microscopy

Aaron C. Johnston-Peck^{*†}, Wei-Chang D. Yang^{‡#}, Jonathan P. Winterstein[‡], Renu Sharma[‡], and Andrew A. Herzing^{*†}

[†]Material Measurement Laboratory, National Institute of Standards and Technology, Gaithersburg, MD 20899, USA

[‡]Center for Nanoscience and Technology, National Institute of Standards and Technology, Gaithersburg, MD 20899, USA

[#]Maryland NanoCenter, University of Maryland, College Park, MD 20742, USA

*Corresponding Authors:

aaron.johnston-peck@nist.gov (A.C. Johnston-Peck)

andrew.herzing@nist.gov (A.A. Herzing)

Material Measurement Laboratory, National Institute of Standards and Technology, 100 Bureau Drive Mailstop 8372, Gaithersburg, MD 20899, USA

Disclaimer: Certain commercial equipment, instruments, or materials are identified in this paper in order to specify the experimental procedure adequately. Such identification is not intended to imply recommendation or endorsement by the National Institute of Standards and Technology, nor is it intended to imply that the materials or equipment identified are necessarily the best available for the purpose.

Table of Contents

	Page Number
Figure S1. Domain formation of C-Ce ₂ O ₃ via repeated reduction cycles	4
Figure S2. RGA background gas analysis from ESTEM	5
Table S1. Ionization cross sections of different molecules	5
Figure S3. Surface terminations of CeO ₂ nanocubes	6
Figure S4. Additional time series of a CeO ₂ nanocube oxidizing	7
Figure S5. Additional time series of a CeO ₂ nanocube oxidizing	8
Figure S6. Additional time series of a CeO ₂ nanocube oxidizing	9
Figure S7. Additional time series of a CeO ₂ nanocube oxidizing	10
Figure S8. Surface terminations of CeO ₂ truncated octahedra	11
Figure S9. Additional time series of a CeO ₂ truncated octahedron oxidizing	12
Figure S10. Additional time series of a CeO ₂ truncated octahedron oxidizing	13
Figure S11. Model of fraction of surface sites for cube and truncated octahedron geometries ...	14
Diffusion simulations by the finite element method	15
Figure S12. Diffusion simulations of a cube geometry	17
Figure S13. Diffusion simulations of a truncated octahedron geometry	19
Kinetic measurements by electron energy loss spectroscopy	19
Figure S14. While-line ratios from oxidizing and reducing particles.....	20
Table S2. Experimental conditions used for collecting data in Figure S14 and S15.....	20
Figure S15. While-line ratios from oxidizing and reducing particles.....	21
Figure S16. Oxidation state measurements on a nanocube as a function of dose rate in the ESTEM	22
Table S3. Rate comparison of gas molecule and electron interactions.....	22
Figure S17. Surface reduction of a CeO ₂ nanocube coated in carbon	23
Figure S18. Oxidation state measurements on a nanocube as a function of temperature	24
Figure S19. Figure 2 from the main text without dashed-line overlays	25
Movie descriptions	25
References	26

Acronyms

Electron energy loss spectroscopy – EELS

Environmental scanning transmission electron microscopy – ESTEM

Fast Fourier transform – FFT

High-angle annular dark field scanning transmission electron microscopy – HAADF-STEM

Low-angle annular dark field scanning transmission electron microscopy – LAADF-STEM

Residual gas analyzer – RGA

Spectrum image – SI

Data provenance

Data shown in Figures S1, S3 to S9, S14, S15, and S17 to S19 was recorded on an FEI Titan 80-300. Data shown in Figures S2 and S16 and was recorded on an FEI Titan ESTEM

White-line ratio calculation

The white-line ratio of the Ce M₅ to the Ce M₄ peak was calculated by taking the second derivative of the spectra and integrating the positive portion of each edge. This was implemented in Digital Micrograph (Mitchell and Schaffer, 2005). The uncertainty of these values is defined as,

$$\delta W = W \sqrt{\left(\frac{\sqrt{N_1}}{N_1}\right)^2 + \left(\frac{\sqrt{N_2}}{N_2}\right)^2}$$

where W is the white-line ratio and N_1 and N_2 are the integrated intensities of the Ce M_{4,5} edges.

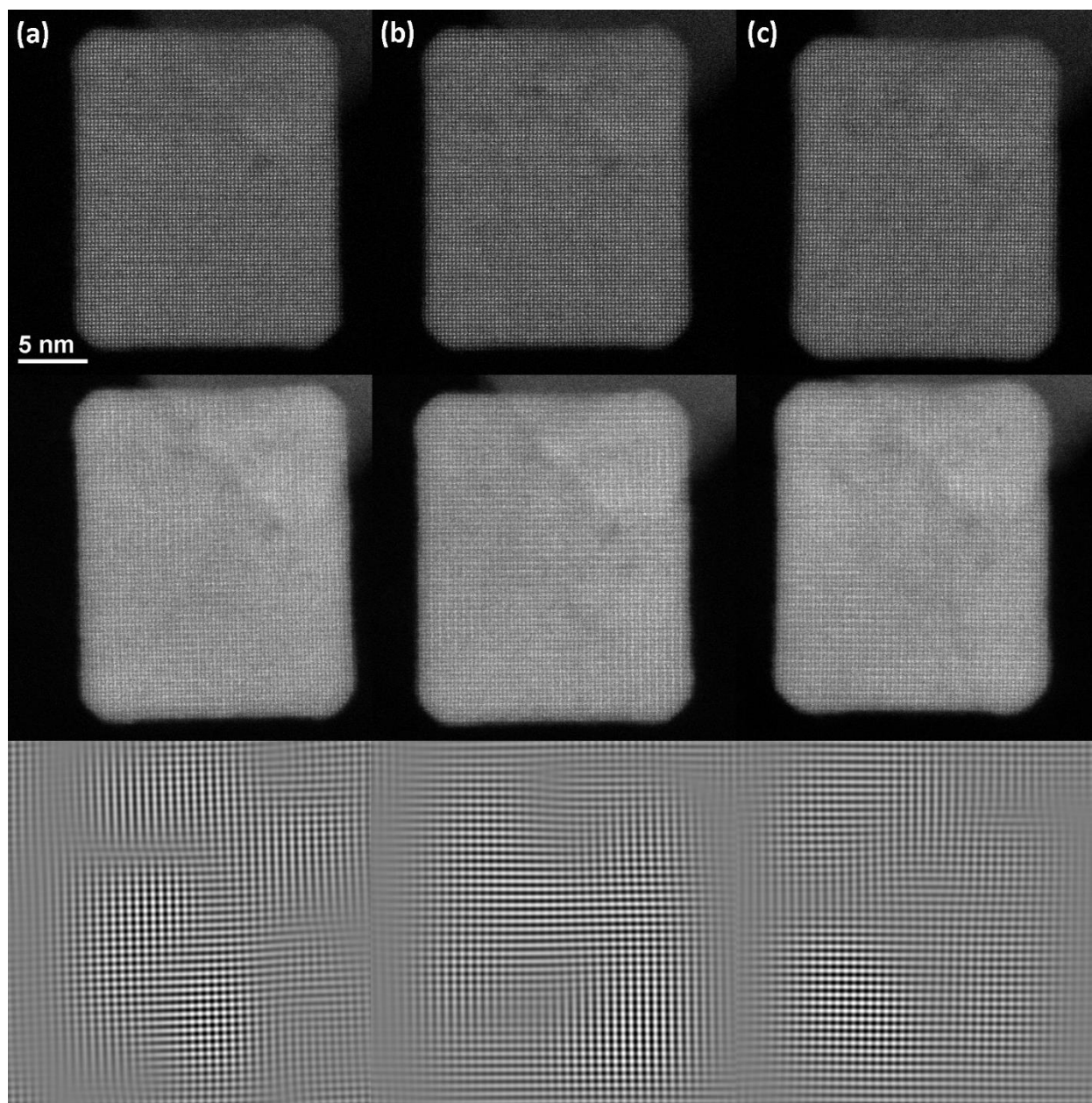


Figure S1. HAADF-STEM images from three separate reduction cycles from the same CeO_2 nanocube (a-c) oriented to a $\langle 001 \rangle$ zone axis. The topmost row depicts the particle at the beginning of the cycle. The middle row of images shows the particle after approximately 200 frames (≈ 1 sec/frame) at a dose rate of $1.65 \times 10^6 \text{ e}^- \cdot \text{nm}^{-2} \cdot \text{s}^{-1}$ (probe current of $\approx 181 \text{ pA}$). Here the C- Ce_2O_3 phase has formed and multiple domains are present. The bottom row is the inverse FFT of the frequencies associated with the $\{020\}$ and $\{200\}$ reflections of the C- Ce_2O_3 phase, same as the procedure described in Figure 4. This highlights the C- Ce_2O_3 domain structure and how it is different for each reduction cycle. Therefore, even though the particle and beam conditions are nominally the same the nucleation and growth of C- Ce_2O_3 domains is not consistent for these conditions.

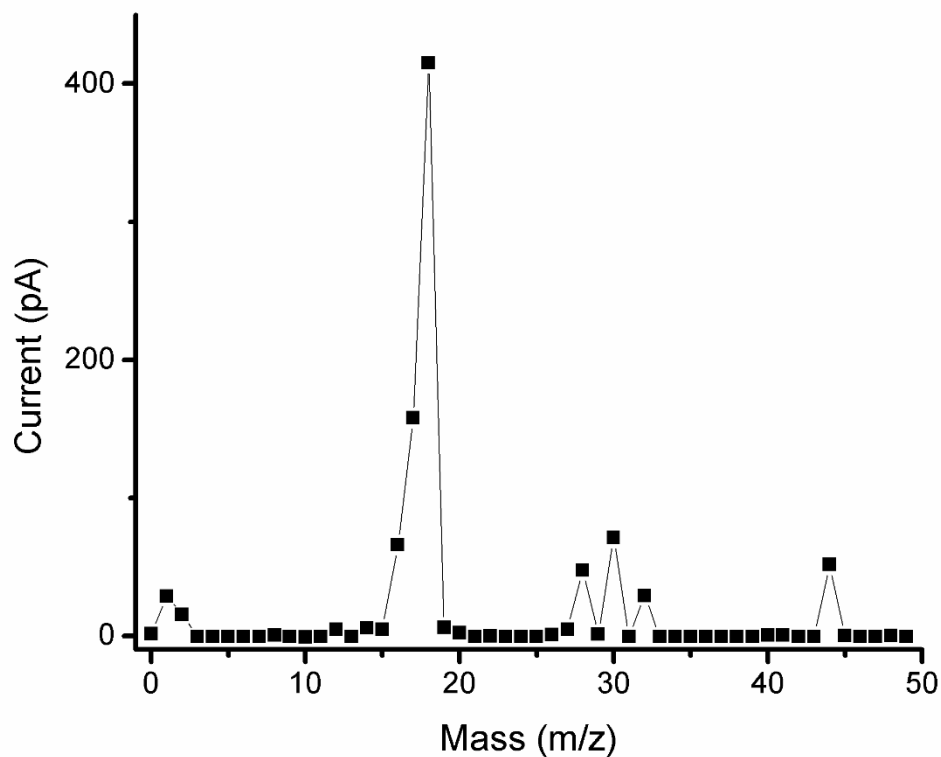


Figure S2. RGA data of the background gases present in the FEI Titan ESTEM used in these studies. Mass to charge (m/z) peaks can be observed at 1,2, 12, 16, 17, 18, 28, 30, 32, and 44. The m/z peaks can correspond to: 1 – H^+ ; 2 – H_2^+ ; 12 – C^+ ; 16 – O^+ ; 17 – OH^+ ; 18 – H_2O^+ ; 28 – CO^+ or N_2^+ ; 30 – NO^+ ; 32 – O_2^+ ; 44 – CO_2^+ . Doubly ionized species or hydrocarbons were not included in this list but may contribute. The most intense peak occurs at m/z value of 18 which corresponds to water.

Table S1. Ionization cross sections of different molecules for electrons with an energy of 70 eV.(Kim et al., 2004)

Specie	Cross Section (nm ²)
H ₂	0.01021
H ₂ O	0.02275
O ₂	0.02441
N ₂	0.02508
CO	0.02516
NO	0.02807
CO ₂	0.03521

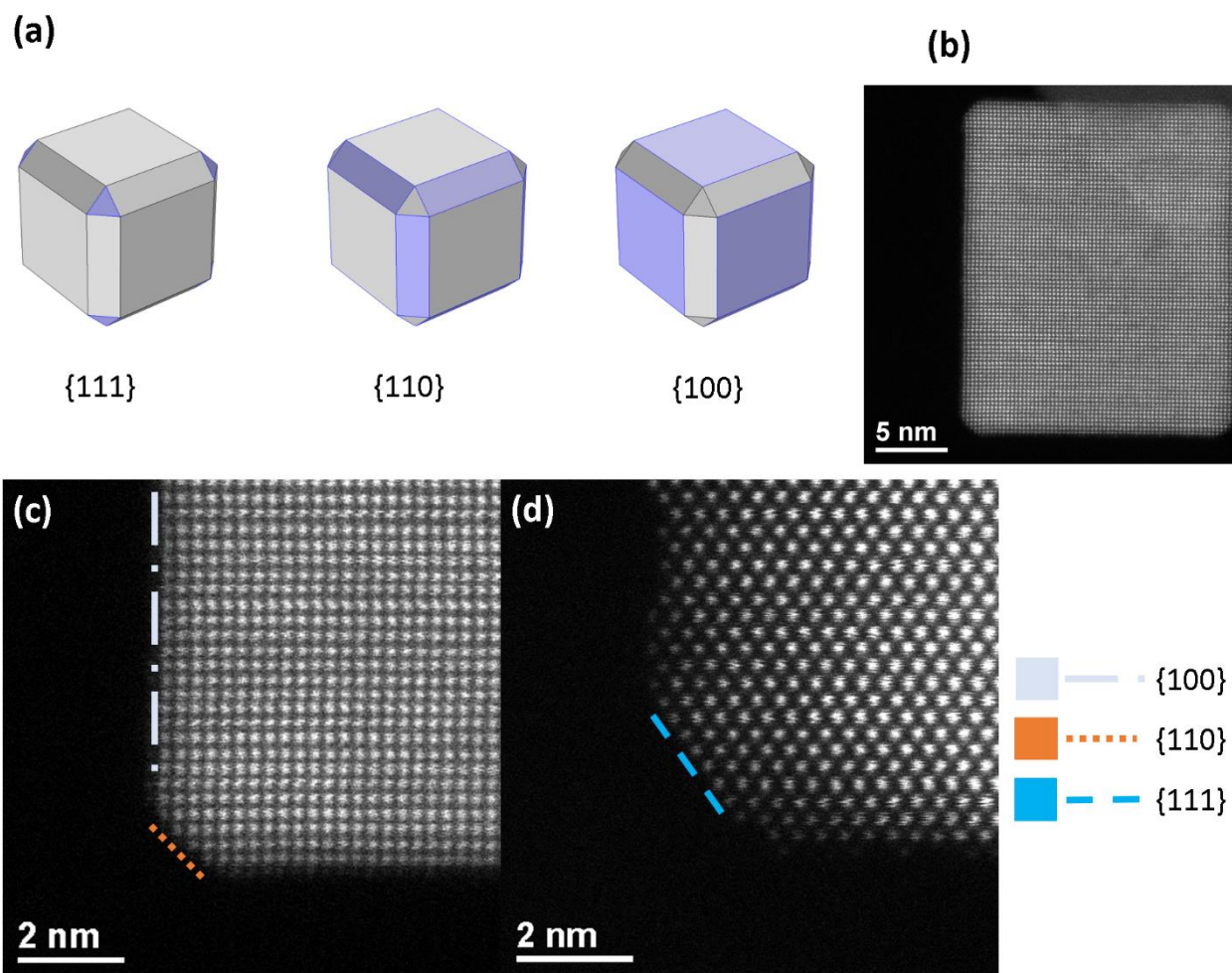


Figure S3. A model depicting the surface terminations of the CeO_2 nanocubes (a). HAADF-STEM images of a nanocube (b) and enlarged images of the nanocube orientated to a $\langle 100 \rangle$ (c) and $\langle 110 \rangle$ (d) zone axis. An example of $\{100\}$, $\{110\}$, and $\{111\}$ terminations are color coded in the images.

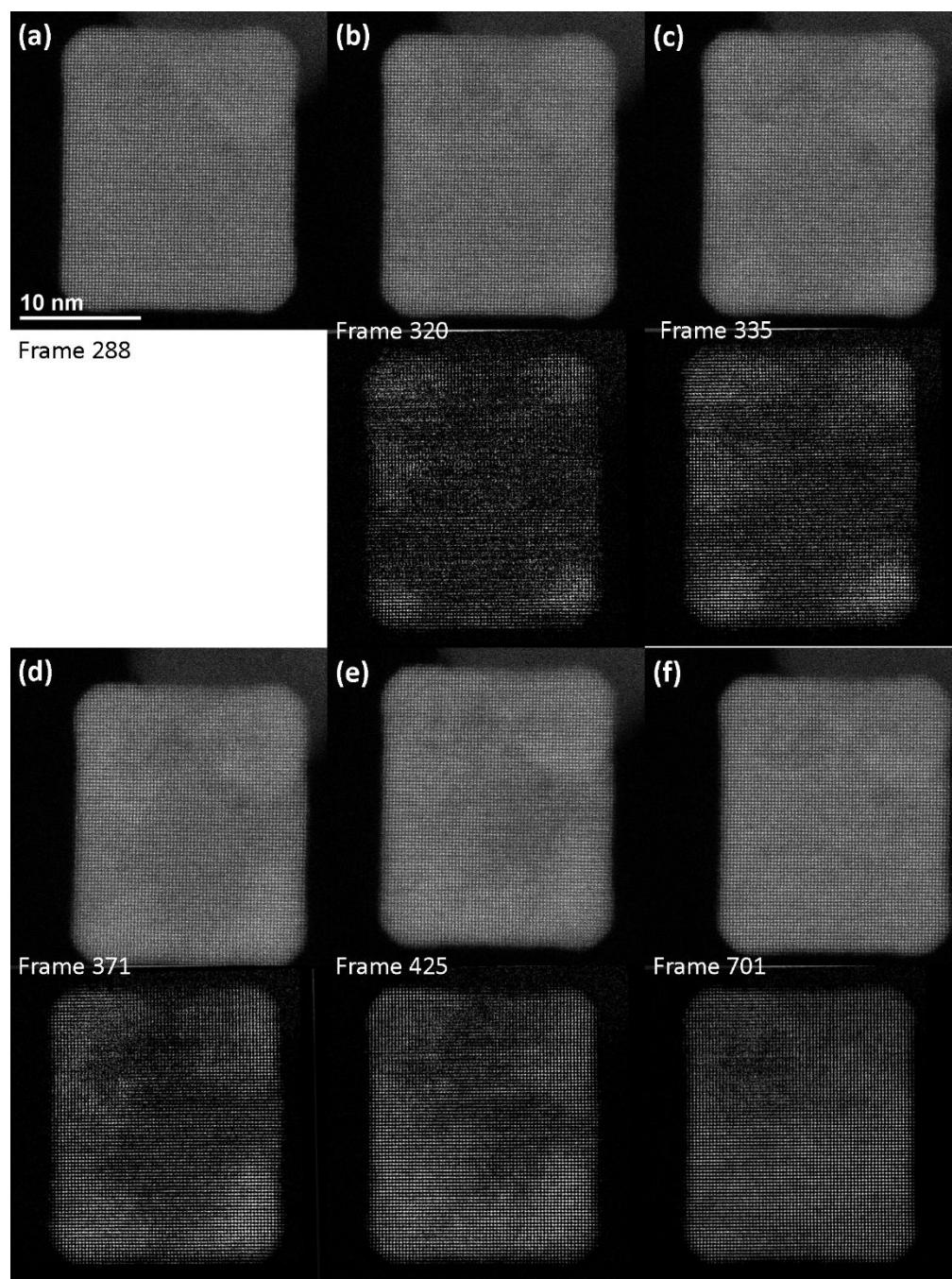


Figure S4. Time series of a reduced nanocube oxidizing from CeO_{2-x} to CeO_2 . Select frames are shown. The increase in intensity from (a) is shown (b-f) below the original image. This contrast indicates regions that are oxidizing. This series of images was taken from the same particle as shown in Figure 5 and Figure S5. The nominally the same dose rate was used and the behavior observed was qualitatively the same, indicating the process is repeatable. Images were recorded using a dwell time of $0.8 \mu\text{s}$ which corresponds to a frame time of approximately 1s.

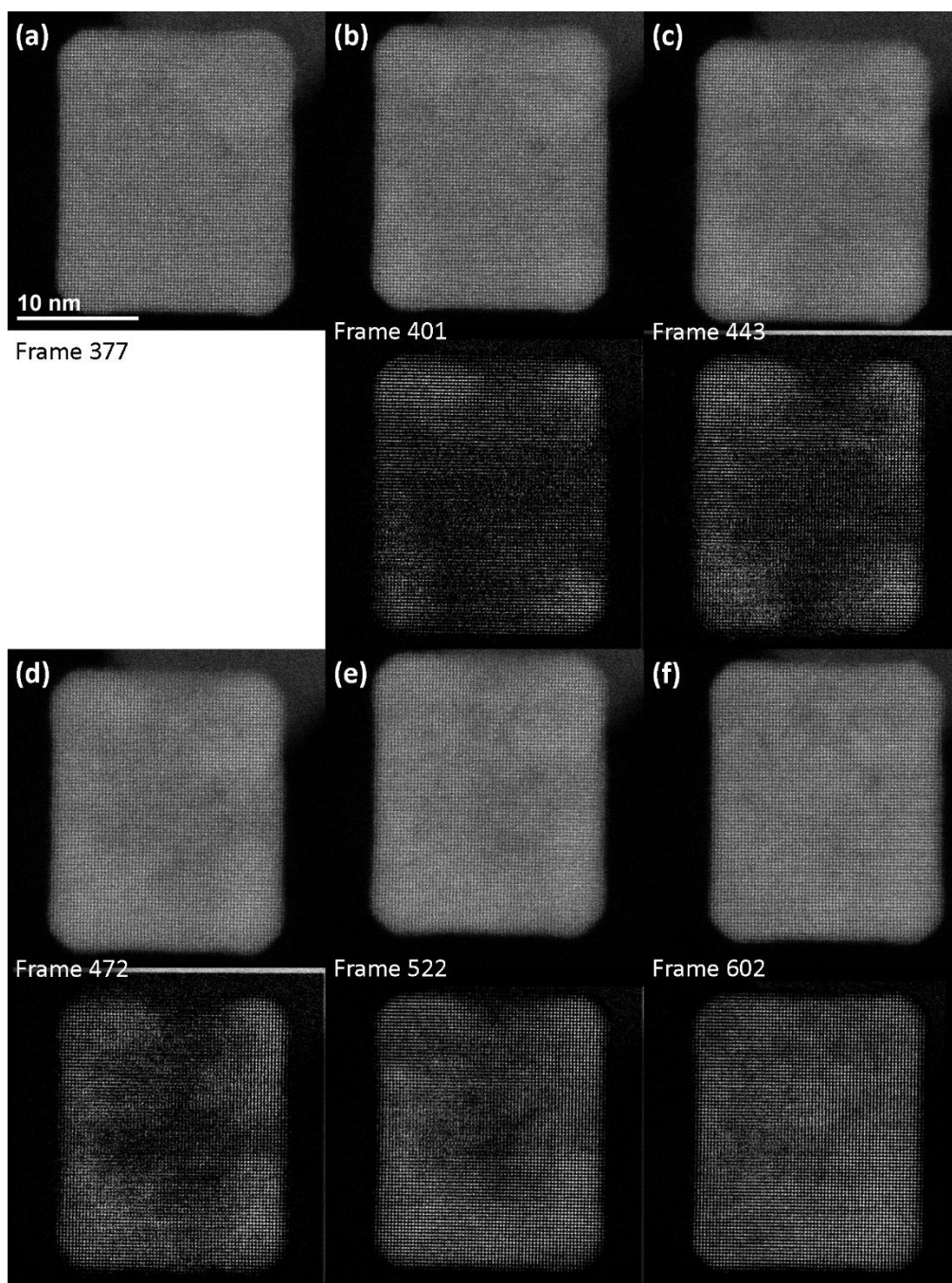


Figure S5. Time series of a reduced nanocube oxidizing from CeO_{2-x} to CeO_2 . Select frames are shown. The increase in intensity from (a) is shown (b-f) below the original image. This contrast indicates regions that are oxidizing. This series of images was taken from the same particle as shown in Figure 5 and Figure S4. The nominally the same dose rate was used and the behavior observed was qualitatively the same, indicating the process is repeatable. Images were recorded using a dwell time of $0.8 \mu\text{s}$ which corresponds to a frame time of approximately 1s.

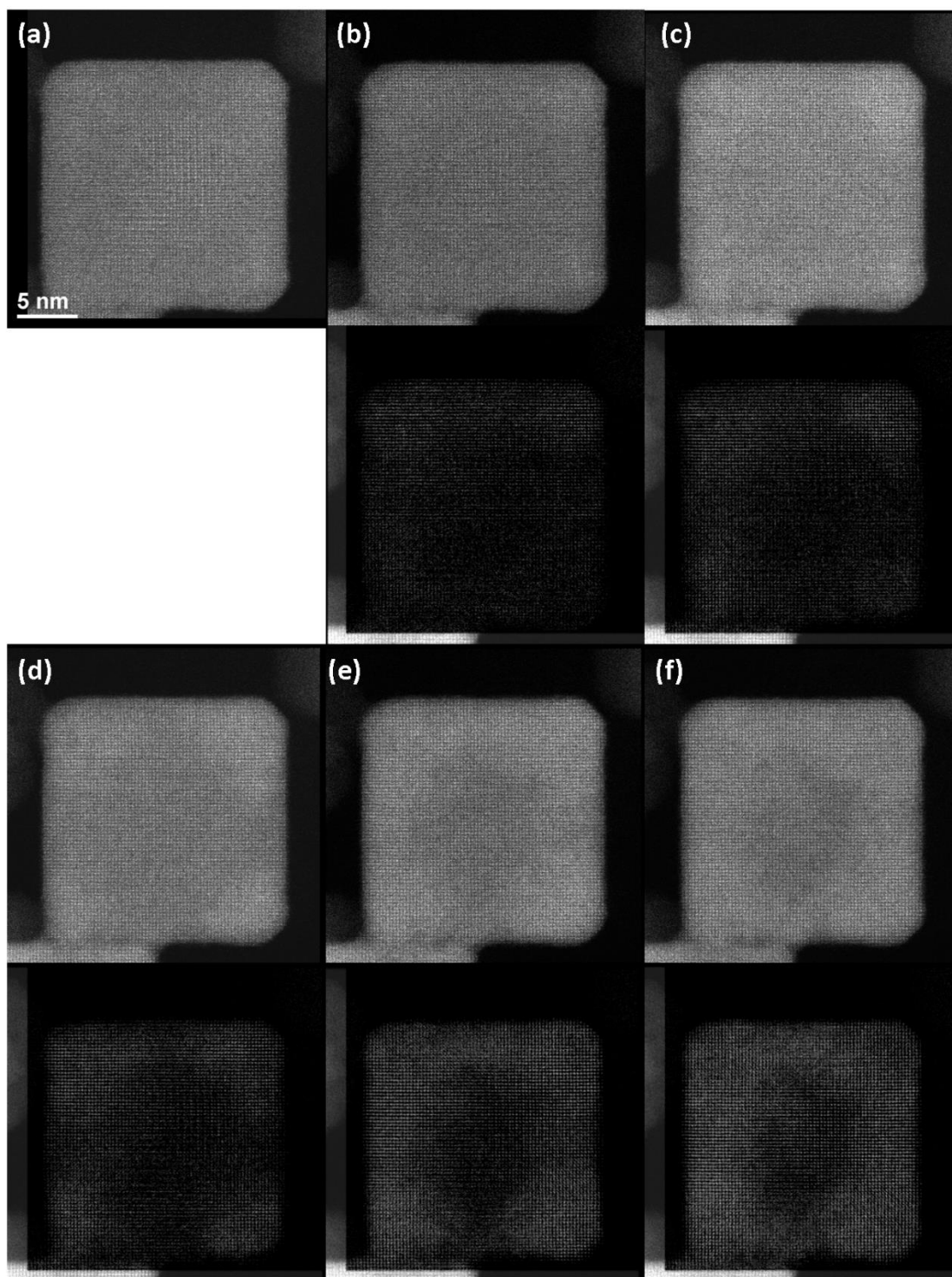


Figure S6. Time series of a reduced nanocube oxidizing from CeO_{2-x} to CeO_2 . Select frames are shown. The increase in intensity from (a) is shown (b-f) below the original image. This contrast indicates oxidizing regions. Data acquisition ceases before reoxidation is complete leaving the central portion less intense, as seen in (f). Images were recorded using a dwell time of $0.8 \mu\text{s}$ which corresponds to a frame time of approximately 1s.

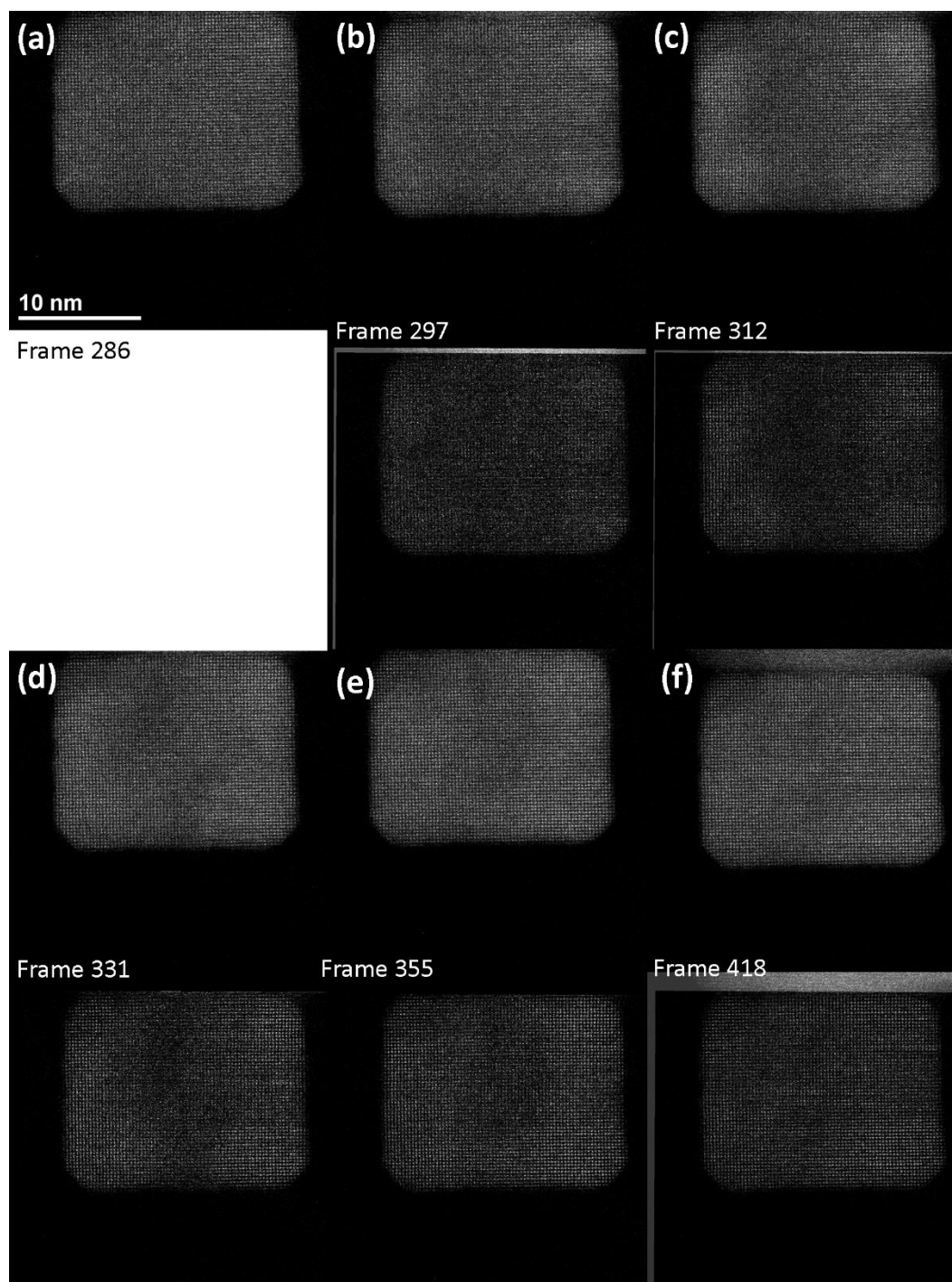


Figure S7. Time series of a reduced nanocube oxidizing from CeO_{2-x} to CeO_2 . Select frames are shown. The increase in intensity from (a) is shown (b-f) below the original image. This contrast indicates oxidizing regions. Images were recorded using a dwell time of $0.8 \mu\text{s}$ which corresponds to a frame time of approximately 1s.

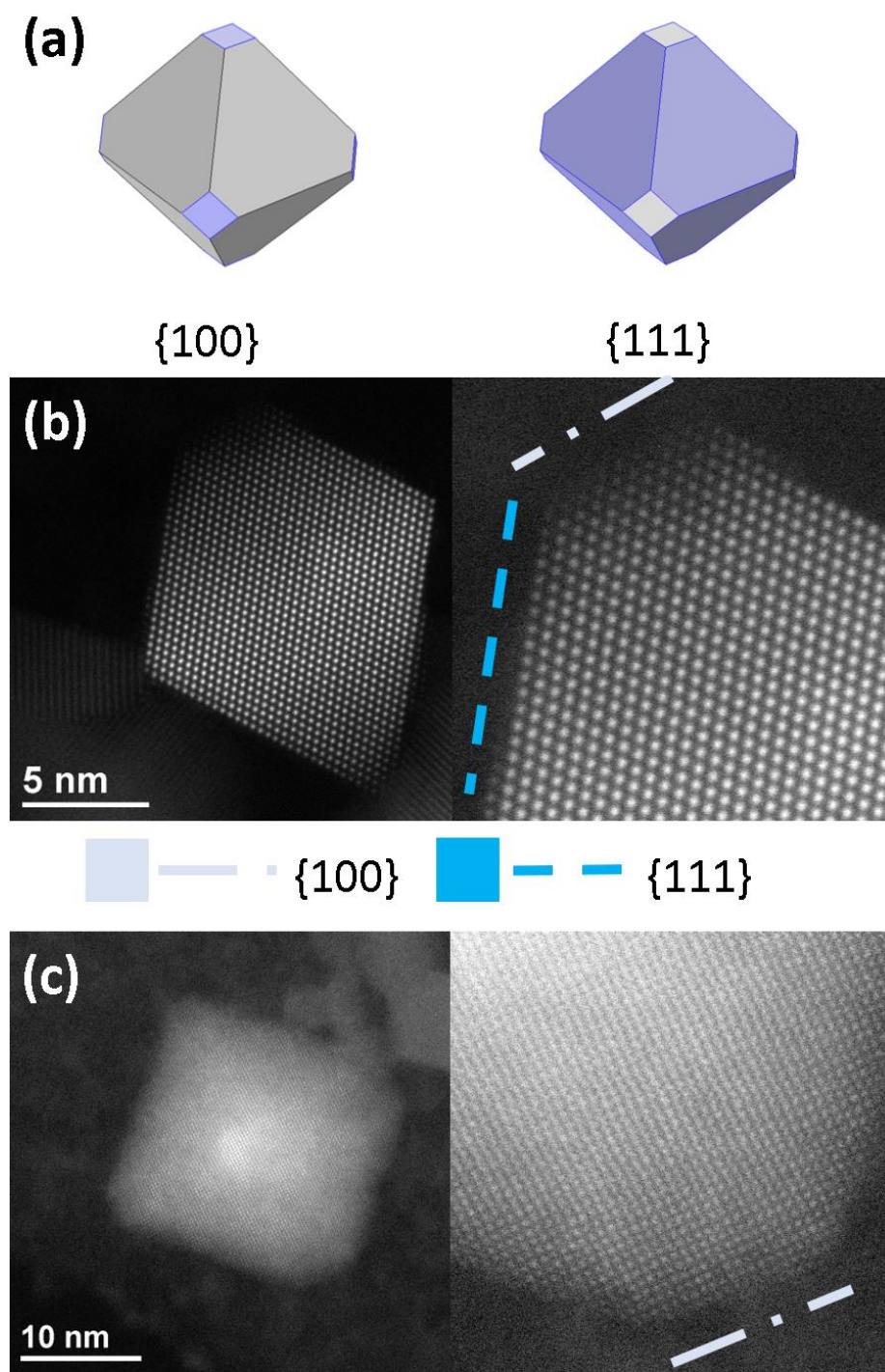


Figure S8. A model depicting the surface terminations of the CeO_2 truncated octahedron. HAADF-STEM images of a truncated octahedra oriented along a $\langle 110 \rangle$ (b) and $\langle 100 \rangle$ (c) zone axis. Enlarged subregions of the particles with examples of $\{100\}$ and $\{111\}$ terminations are color coded. Gamma adjustments were applied to the images to increase visibility of the facets. Images in (b) are the sum of a series of images that were aligned using a rigid body registration as implemented by StackReg in FIJI (Schindelin et al., 2012; Schneider et al., 2012; Thevenaz et al., 1998).

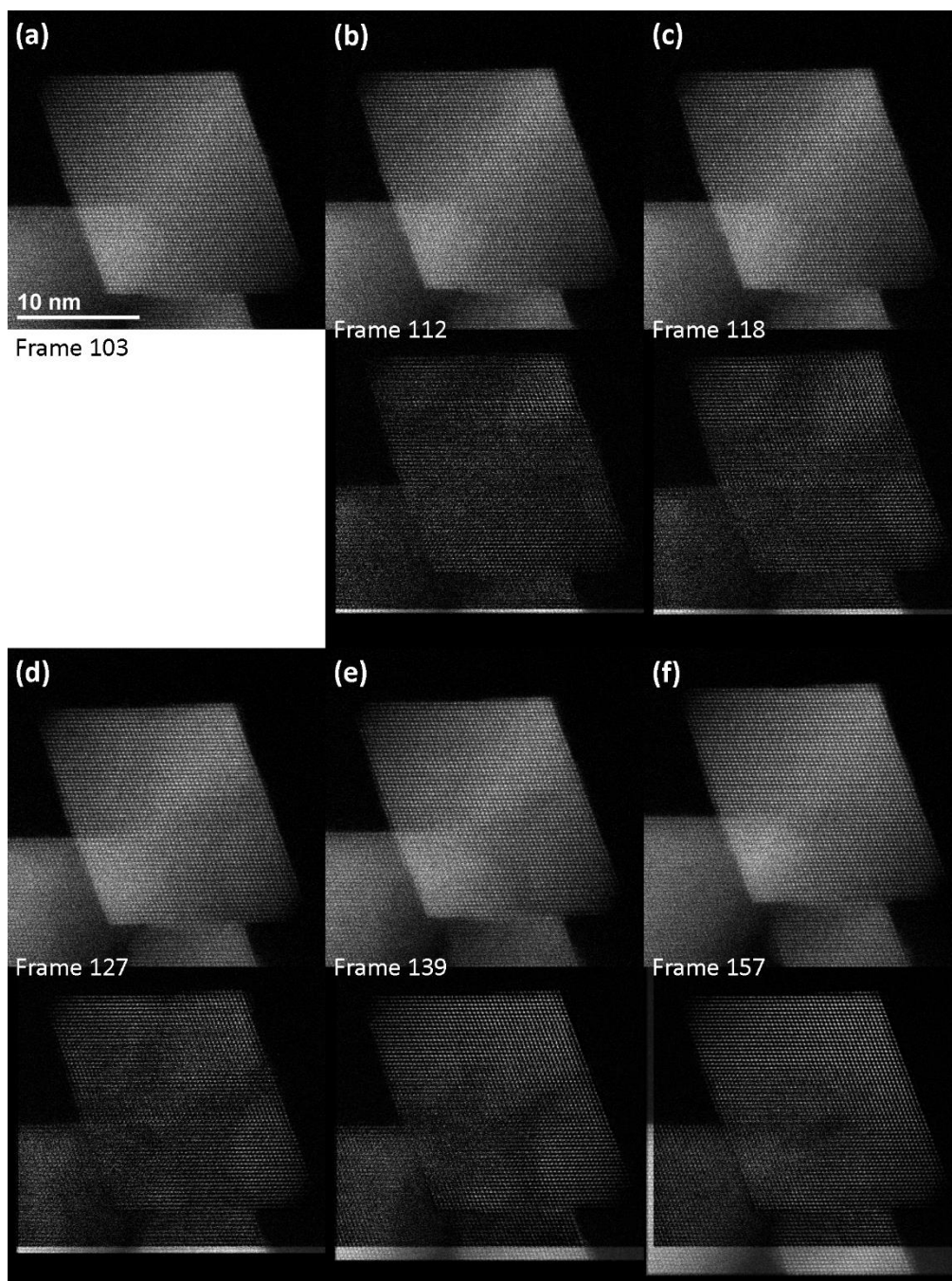


Figure S9. Time series of a reduced truncated octahedron from CeO_{2-x} to CeO_2 . Select frames are shown. The increase in intensity from (a) is shown (b-f) below the original image. This contrast indicates oxidizing regions. This series of images was taken from the same particle as shown in Figure 6. The nominally the same dose rate was used and the behavior observed was qualitatively the same, indicating the process is repeatable. Images were recorded using a dwell time of $0.8 \mu\text{s}$ which corresponds to a frame time of approximately 1s.

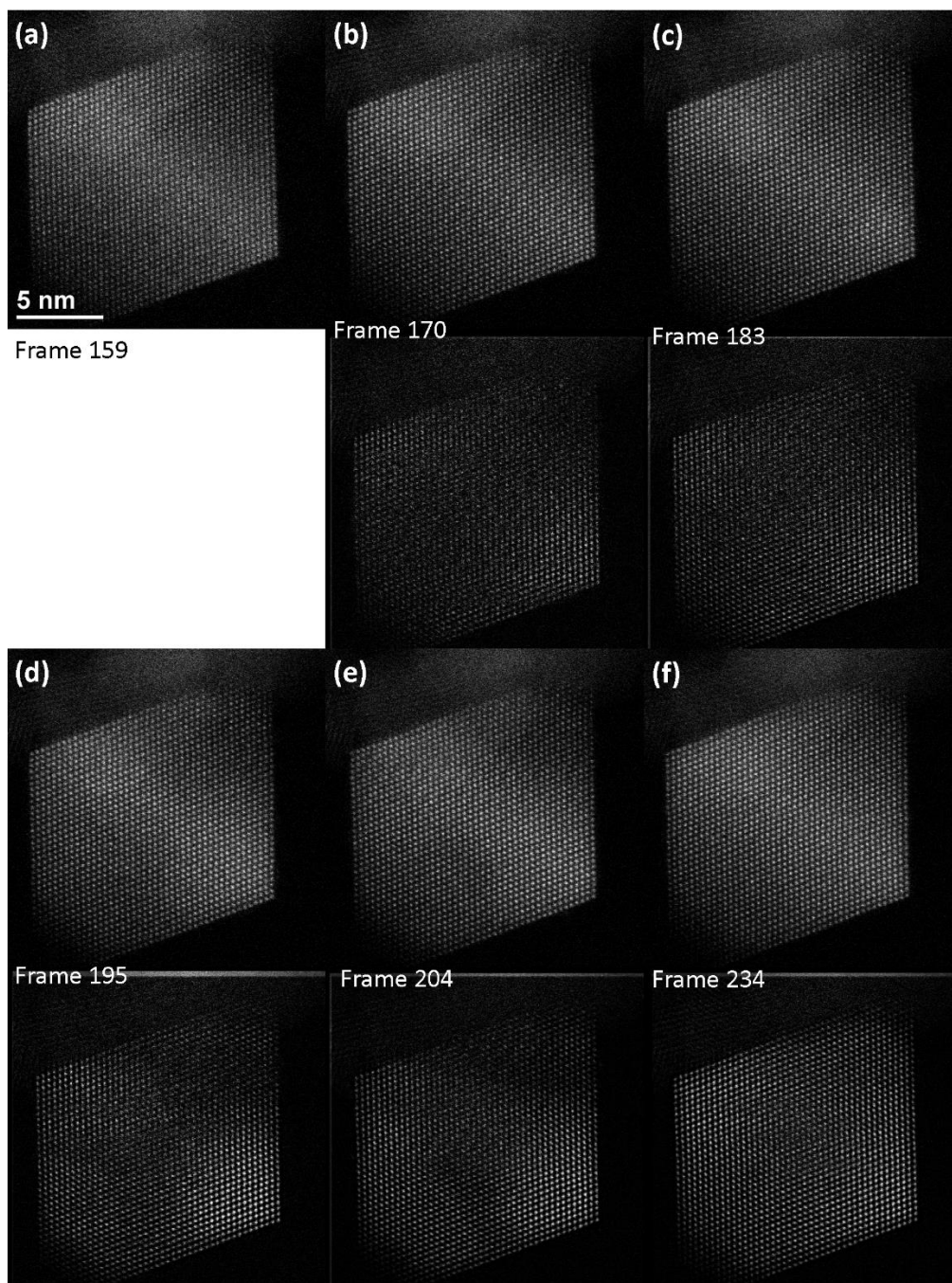


Figure S10. Time series of a reduced truncated octahedron from CeO_{2-x} to CeO_2 . Select frames are shown. The increase in intensity from (a) is shown (b-f) below the original image. This contrast indicates oxidizing regions. Images were recorded using a dwell time of $0.8 \mu\text{s}$ which corresponds to a frame time of approximately 1s.

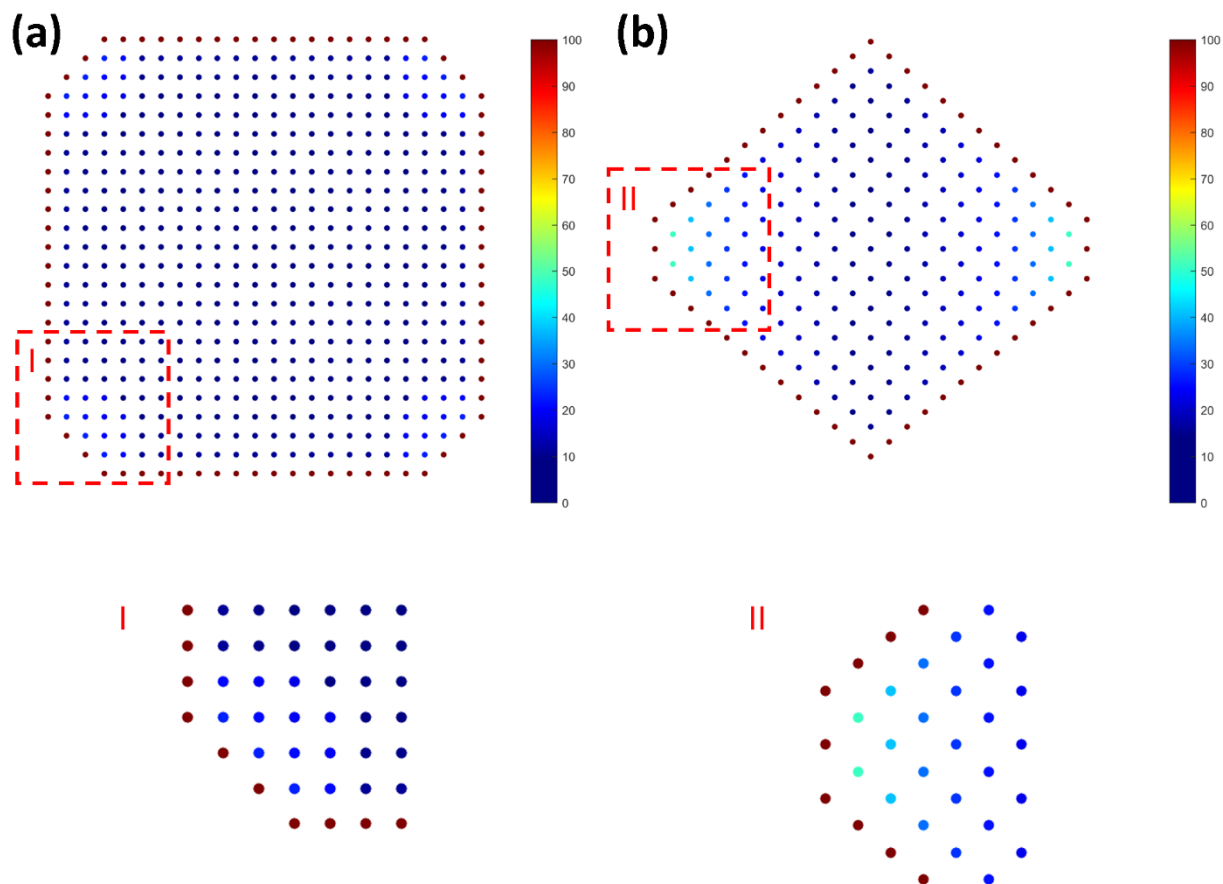


Figure S11. A model depicting a three-dimensional cubic lattice with surface facets that mimic the CeO₂ nanocubes (a) and truncated octahedra (b). Each point, representing a column of atoms, is colorized according to the percentage of atoms within the column that are located at a surface. This illustrates that the diffusion pathways from the surface to bulk in regions bound by corners and tips are shorter than those bound by faces. Corner regions marked by dashed boxes are enlarged and presented below the original model.

Diffusion simulations by the finite element method

Diffusion was simulated in a cube and truncated octahedron geometry using the finite element method as implemented in COMSOL. The intent of the simulations is not to provide a fully quantitative comparison with experimental data but rather capture qualitative spatial differences in concentration as a function of facet activity. The flux of oxygen from the surrounding into the particle volume was systemically tested as a function of facet type. It was assumed that a facet was either active (i.e., flux occurring) or inactive (i.e., no flux) and the same flux rate was used regardless of facet type. The diffusion was treated as isotropic and represented by Fick's Law. Flux of new species into the volume was permitted up to a critical concentration representing the fully oxidized state (i.e., CeO_2) and arbitrary values were selected for the diffusion rate constant and flux rate.

In Figure S12a the cube geometry has surface terminations representing the $\{100\}$, $\{110\}$ and $\{111\}$ facets. Species were permitted to diffuse through the facets individually or collectively. Snapshots from the simulations results are plotted as an isosurface representing a concentration threshold. These isosurfaces can be compared with the HAADF-STEM data recorded during oxidation and the isosurface could be envision as a concentration threshold at which a contrast change in the HAADF image would result, analogous to what was presented in the experimental results as the particles oxidized from CeO_{2-x} to CeO_2 . Therefore, projected volumes entirely outside the isosurface could be perceived as the more intense (oxidized) regions in the HAADF-STEM image. The positions and propagation of the isosurface in Figure S12b-e is similar, although the amount of time (not indicated nor scaled) to reach these different states is different. For the parameters used in the COMSOL simulation, as the area of active surface increases the time necessary for the critical concentration to be reached decreases. Therefore, the case of all the facets being active (S12b) reaches the critical concentration the quickest while the case of only the $\{111\}$ facets being active (S12c) is the slowest. The spatial evolution of the concentration gradient mimics the evolution of the contrast behavior observed in the HAADF-STEM data. That is, it oxidizes more quickly in regions bounded by the corners. However, when transport is permitted through only the $\{100\}$ surfaces (Figure S12f) the behavior is different from the other simulations and does not mimic the HAADF-STEM data. In this case the contrast change would be expected to occur initially along the faces of the cube rather than the corners (which was experimentally observed). This analysis suggests that the dissociation of gases and incorporation of oxygen does not occur solely on the $\{100\}$ surfaces and must proceed by another mechanism involving other surfaces and one that may or may not include $\{100\}$ surfaces.

This analysis was repeated for the truncated octahedron geometry. In Figure S13a the model has surface terminations representing the $\{100\}$ and $\{111\}$ facets. Like in the cube, a time dependence was also observed with the case of all facets being active (Figure S13b) reaching the critical concentration quickest and the case of only $\{100\}$ facets being active (Figure S13c) being the slowest to reach the critical concentration. The snapshots from all three

cases demonstrated similar spatial evolution of the isosurface where the concentration increases quickest in regions bound by particle tips. This behavior mimics what was experimentally observed in the HAADF-STEM data. But because the isosurface evolves similarly for all three simulations no clear differentiation between the facets can be made with this information. Meaning that the *spatial evolution of anion deficient regions* observed in the truncated octahedra HAADF-STEM datasets is dominated by the particle shape (geometry effect) and is relatively insensitive to the ability of surfaces to absorb oxygen from gases in the environment (facet effect). However, differences as a function of the *facet effect* would still manifest themselves in kinetic data on the reduction and oxidation of the particle. An outcome which we do observe in the kinetic measurements (see below).

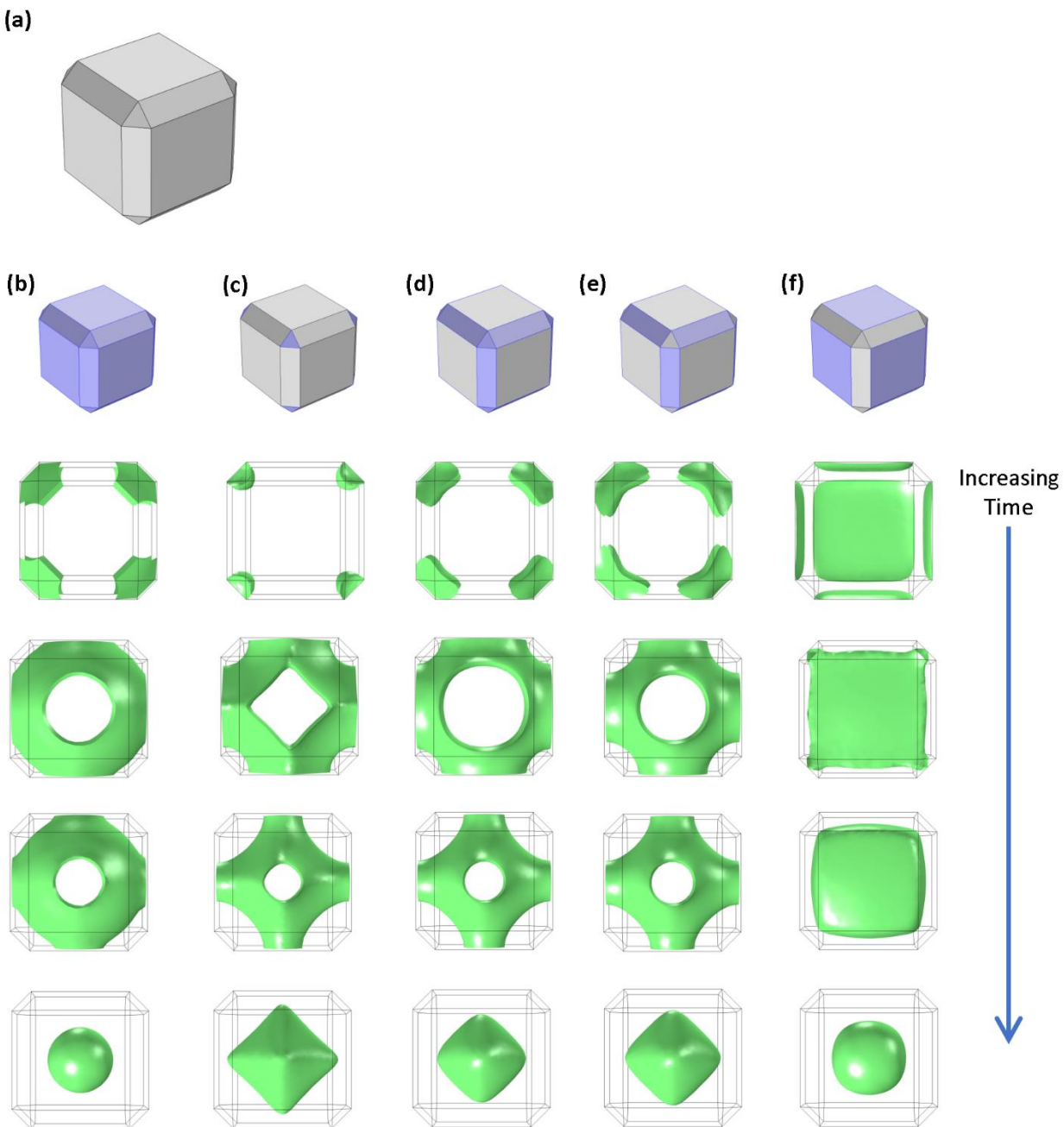


Figure S12. Diffusion simulations in a cube whose geometry mimics $\{111\}$, $\{110\}$, and $\{100\}$ surface terminations (a). Flux into the cube was systemically adjusted to all surfaces (b), $\{111\}$ (c), $\{110\}$ and $\{111\}$ (d), $\{110\}$ (e), and $\{100\}$ (f). The green isosurface identifies the position of a concentration threshold as it changes with time. The spatial evolution of the isosurface is similar for (b-e) while $\{100\}$ only (f) differs from the other combinations.

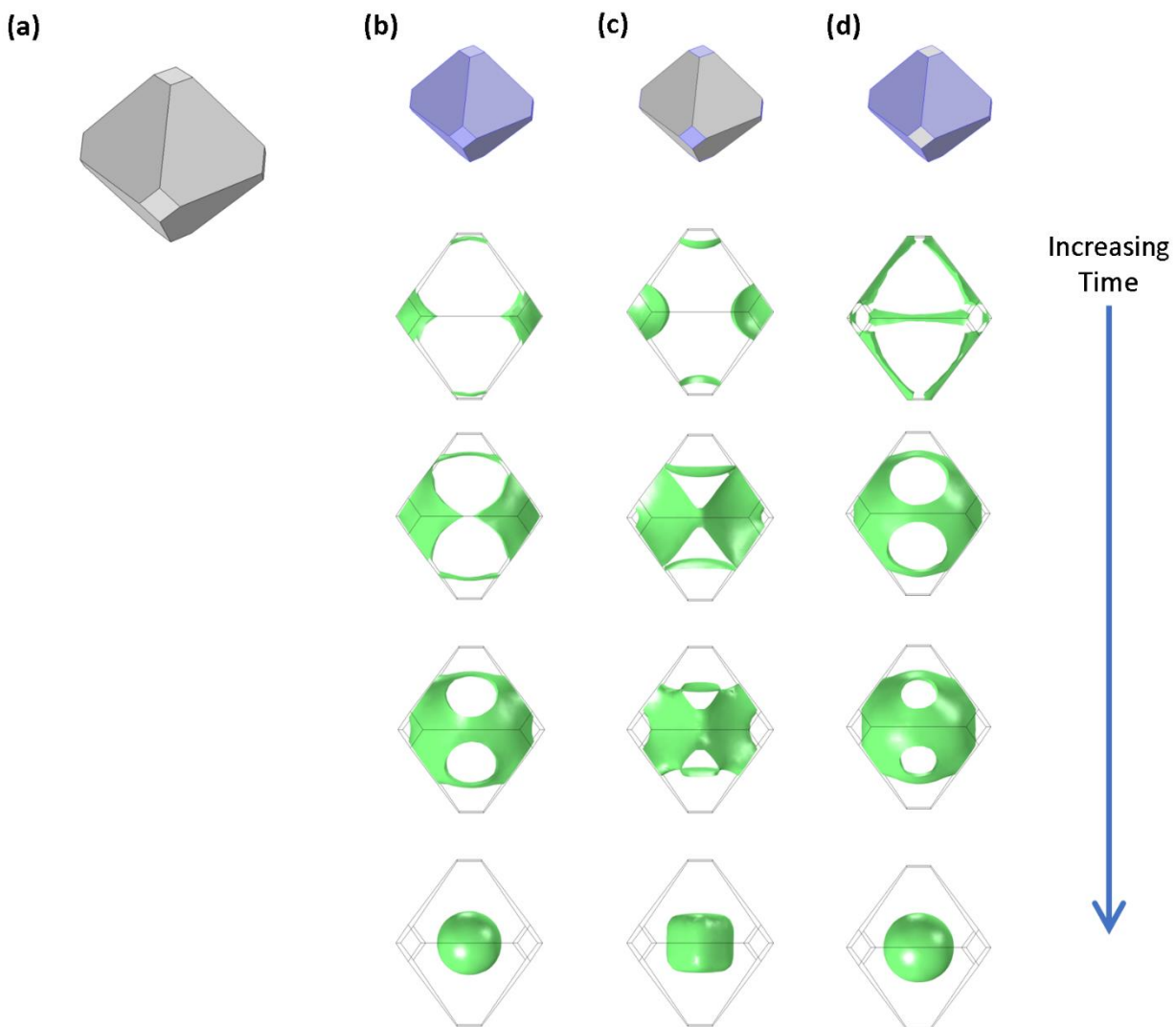


Figure S13. Diffusion simulations in a truncated octahedron whose geometry mimics $\{111\}$ and $\{100\}$ surface terminations (a). Flux into the cube was systemically adjusted to all surfaces (b), $\{111\}$ (c), and $\{100\}$ (d). The green isosurface identifies the position of a concentration threshold as it changes with time. The spatial evolution of the isosurface is similar for all cases (b-d).

Kinetic Measurements by Electron Energy Loss Spectroscopy

Direct comparisons in kinetic behavior, the rate at which the particles were reduced by the electron beam or oxidized in the background gases of the microscope, of nanocubes versus truncated octahedra were made. The comparisons were made by controlling for irradiation conditions by using the same dose rate (i.e., same dwell time, magnification, and probe current) and nominally the same gas environment. This was achieved by loading the both types of particles onto the same TEM grid and waiting several hours after the sample was loaded to allow the microscope environment to stabilize. The general scheme for the data acquisition was the particles were first exposed to a dose rate below the critical-dose rate threshold, next the dose rate was increased past the critical-dose rate threshold reducing the particles, last the dose rate was reduced back to the initial dose rate allowing the particles to oxidize (Figure S14a). EELS spectra were recorded and the white-line ratio was then calculated and plotted. From the experimental conditions and data processing parameters used here a white-line ratio value of ≈ 0.92 corresponds to Ce^{+4} (fully oxidized) and a value of ≈ 1.27 corresponds to Ce^{+3} (fully reduced).

In Figure S14b the white-line ratio is plotted as a function of time using exposure conditions described in Table S2. The time at which the dose-rate transitions were made is slightly different for each particle. Therefore, the data was replotted setting the origin at the transition point for when the dose rate was increased above the critical-dose rate threshold (Figure S14c) and when the dose rate was returned below the critical-dose rate threshold (Figure S14d). The data was fit using exponential equations of the form $y = y_0 + Ae^{kx}$ where k (either positive or negative) is a time constant sensitive to how quickly the reaction proceeds and y_0 represents the limit of the reaction. Under the high dose rate conditions (Figure S14c) the magnitude of k was approximately twice larger for nanocubes indicating a faster rate of reduction than truncated octahedra. Under oxidizing conditions (Figure S14d) the magnitude of k was approximately four times larger for truncated octahedra indicating a faster rate of oxidation than nanocubes.

In Figure S15 additional data is presented from different particles using three different exposure conditions (S15a-c). The top row depicts the entire experiment while the middle row and bottom row represents the time after the dose rate transitioned from above or below the critical dose rate, respectively. The data was analyzed in the same manner and similar results were found. Under the high dose rate conditions (middle row Figure S15) nanocubes were found to reduce to a greater extent and the magnitude of k was larger for nanocubes indicating a faster rate of reduction than truncated octahedra. Under oxidizing conditions (bottom row Figure S15) the magnitude k was larger for truncated octahedra indicating a faster rate of oxidation than nanocubes.

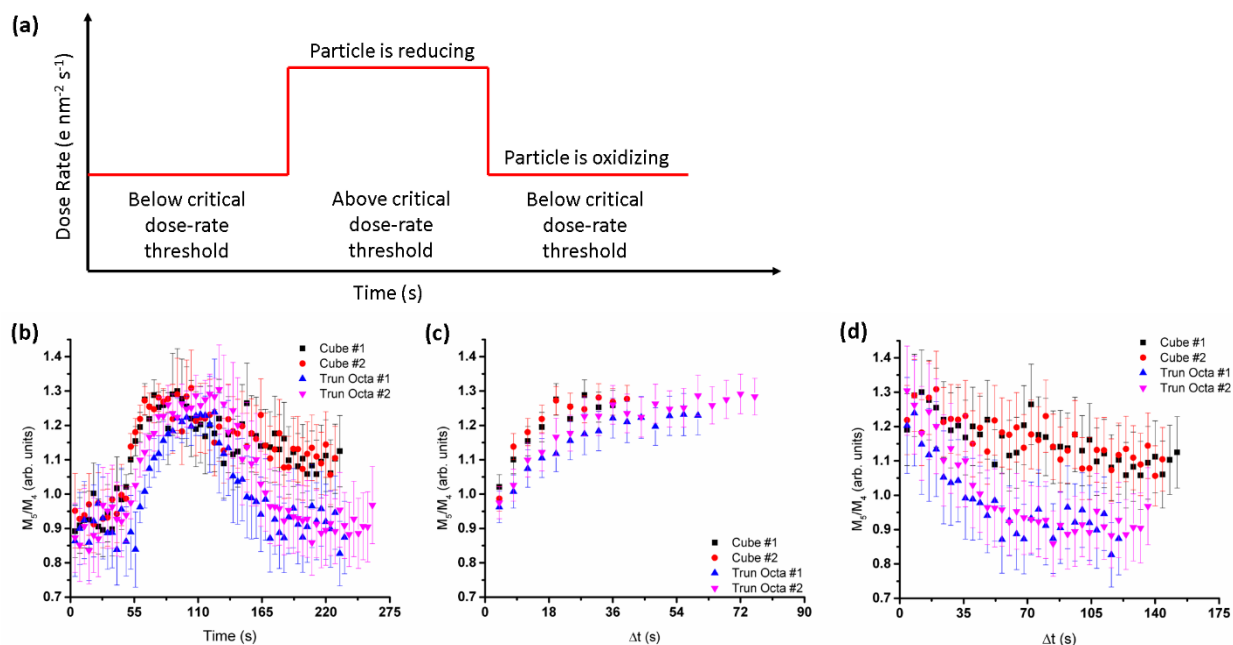


Figure S14. Oxidation and reduction of CeO_2 nanocubes and truncated octahedra. A schematic depicts the change in dose rate as a function of time during these experiments. The white-line ratio is plotted as a function of time (b). Portion of the data is replotted to isolate portions of the data as the particles reduce under a high dose rate (c) and as the particles oxidize under a low dose rate (d).

Table S2. Experimental Conditions used to collect data in Figure S14 and S15

Figure	Dwell (μs)	Raster Size	Image Size (nm)	<i>Below Threshold</i> - Dose Rate/probe current ($\text{e} \cdot \text{nm}^{-2} \cdot \text{s}^{-1}/\text{pA}$)	<i>Above Threshold</i> - Dose Rate/probe current ($\text{e} \cdot \text{nm}^{-2} \cdot \text{s}^{-1}/\text{pA}$)
S14	0.8	1024 x 1024	25.96 x 25.96	$6.95 \cdot 10^5/75$	$4.63 \cdot 10^6/500$
S15a	0.8	1024 x 1024	36.64 x 36.64	$2.79 \cdot 10^5/60$	$2.06 \cdot 10^6/444$
S15b	0.8	1024 x 1024	25.96 x 25.96	$3.71 \cdot 10^5/40$	$3.24 \cdot 10^6/351$
S15c	0.8	1024 x 1024	25.96 x 25.96	$2.78 \cdot 10^5/30$	$2.08 \cdot 10^6/225$

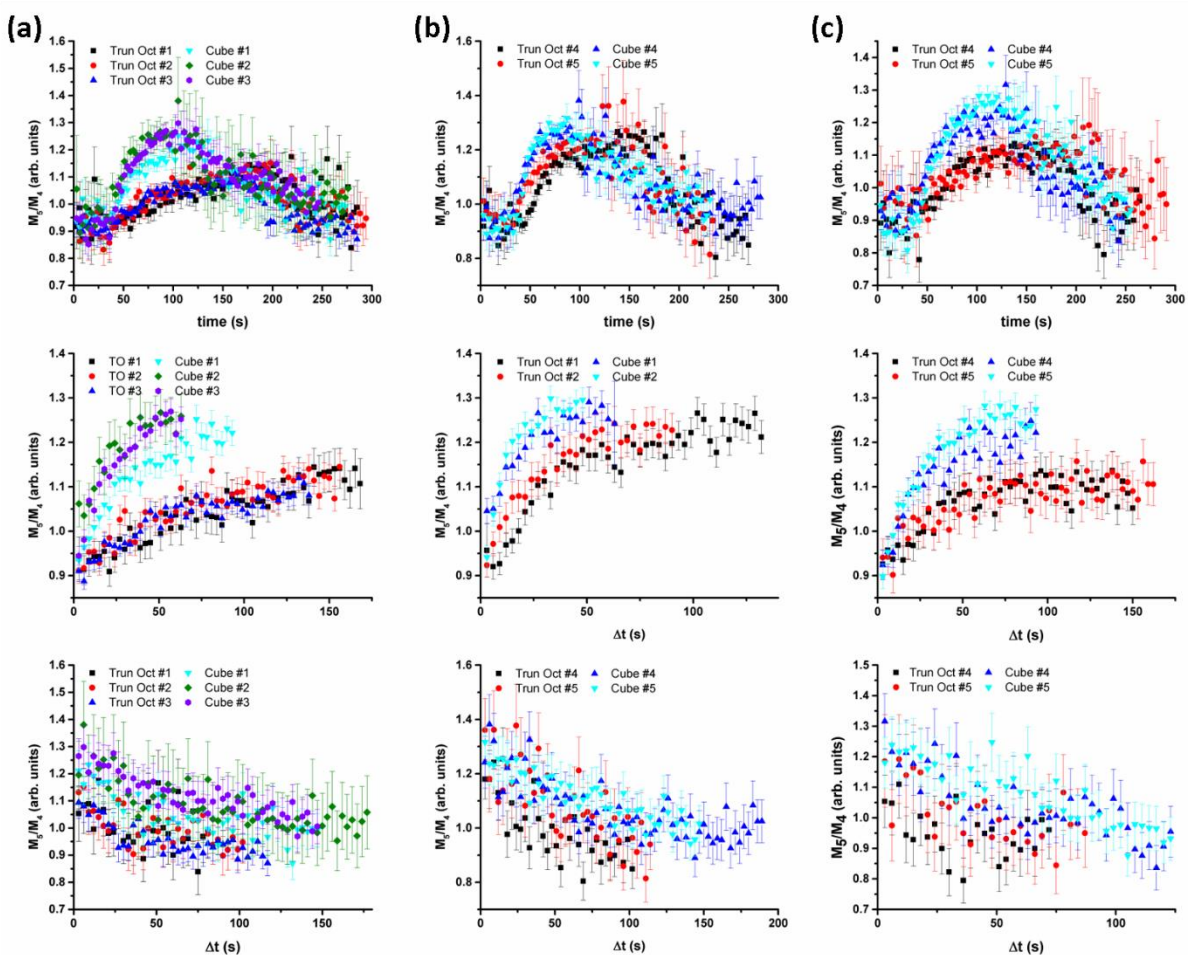


Figure S15. Oxidation and reduction of CeO_2 nanocubes and truncated octahedra. The white-line ratio is plotted as a function of time for three sets of experimental conditions (a-c). The top row displays the entire experiment, the middle row replots the portion of data as the particles reduce under a high dose rate, and the bottom row replots the portion of data as the particles oxidize under a low dose rate.

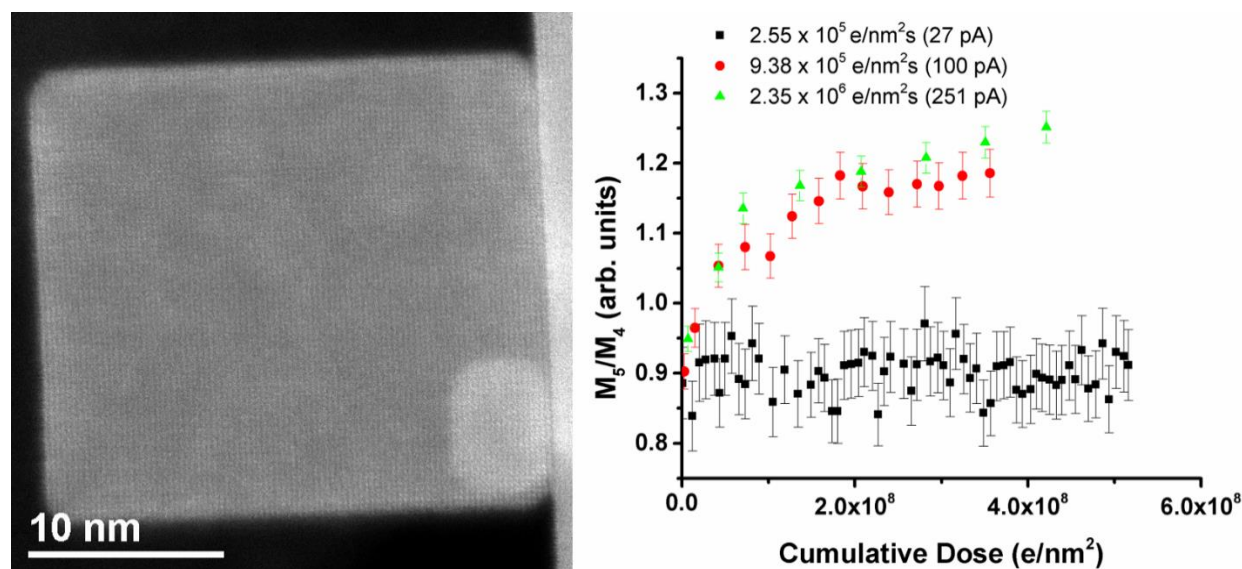


Figure S16. LAADF-STEM image of a CeO₂ nanocube used for ESTEM measurements. The graph shows the white-line ratio as a function of cumulative dose for three different dose rates. These measurements were taken in vacuum. At the lowest dose rate no detectable reduction of the nanocube occurs. At higher dose rates, even though the total cumulative dose is less, the nanocube reduces. Dose-rate-dependent reduction of CeO₂ has been described in detail elsewhere (Johnston-Peck et al., 2016).

Table S3. Duplication of Table 1 with a comparison of gas collisions and incident electrons per second.

Gas	Pressure (Pa)	% Ce ³⁺	σ	Gas molecule collisions (s ⁻¹)	Incident Electrons (s ⁻¹)	Gas Molecules per Electron
Oxygen	≈ 158	0.4	0.8	≈ 3.3E+08	≈ 1.6E+06	≈ 205
Oxygen	≈ 1	4.4	2.3	≈ 2.8E+06	≈ 1.6E+06	≈ 1.7
Vacuum	≈ 2*10 ⁻⁵	11.9	2.5	≈ 36	≈ 1.6E+06	≈ 2.20E-05

The Table S3 calculations assume gas molecules are following the ideal gas law based on collisions with a wall. Particles are assumed to possess a spherical geometry with a diameter of 5 nm. The total atomic elastic scattering cross section of Ce and O with 300 keV electrons is ≈ 1.2E-21 m² and ≈ 4.6E-23 m², respectively (A. Jablonski, 2016). The total inelastic scattering cross sections would be on the same order of magnitude as the elastic cross sections. The sticking coefficient is unknown. Using a kinematic scattering approximation and assuming a sticking coefficient of 0.5, the number of adsorbing molecules per scattered electron would be approximately an order of magnitude greater than the values reported in the column “Gas Molecules per Electron”.

The role of carbon coatings on the presence of reduced surfaces – an additional control experiment

The presence of reduction at surfaces may be a response to the vacuum environment of microscope or the outcome of damaging interactions with the electron beam. A carbon shell encapsulating a CeO₂ particle was previously reported to significantly increase the critical-dose rate threshold thereby inhibiting beam damage (Johnston-Peck et al., 2016). Here a carbon shell was deposited in situ before recording the spectrum image. As the electron beam is scanned it cracks hydrocarbons present on the sample depositing an amorphous carbon coating over the CeO₂ nanocube. A low dose rate was used to deposit the carbon. This dose rate was less than the dose rate used to record the SI. Once the carbon shell was deposited a SI was recorded. The data was analyzed using EELSModel (Verbeeck and Van Aert, 2004). Ce⁺³ and Ce⁺⁴ reference spectra were fit to the experimental data. Results from the SI are shown in Figure S17. The surface of the nanocube is reduced even though the protection layer was present. If surface reduction did not occur while the carbon shell was deposited, this indicates that the surface became reduced when the particle was introduced into the vacuum environment and not the result of recording the SI (i.e., beam damage).

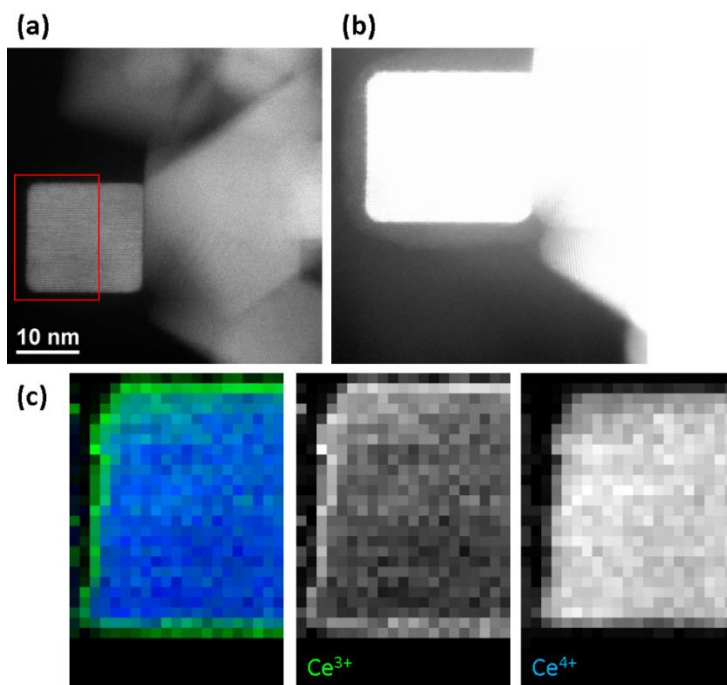


Figure S17. Oxidation state measurement of a CeO₂ nanocube coated in a carbon shell. A HAADF-STEM image shows the cube, the red box indicates the region where the spectrum image was recorded (a). A non-linear histogram adjustment (gamma) and contrast adjustment was made to highlight the carbon (b). Color composite of the Ce³⁺ (blue) and Ce⁴⁺ (green) component maps indicate the particle surface is reduced (c).

The role of temperature on the critical dose rate threshold

Introducing gases, as was done during the ESTEM experiments, may influence the specimen by increasing conductivity of the system thereby tempering the mechanism for electron beam mediated reduction. To explore the role of reduced temperature, oxidation state measurements were recorded as a function of temperature. A Gatan 636 liquid nitrogen holder was used. Data was acquired with the sample at room temperature (≈ 295 K) and cooled by liquid nitrogen (≈ 96 K). The sample was allowed approximately 2 hours to stabilize after introducing liquid nitrogen. Under both temperatures comparable datasets were collected where particles were exposed to identical beam rasters (magnification, dwell time, size) and dose rates as the EEL spectra were recorded. A systematic trend emerged as the cooled nanocubes were more susceptible to electron beam driven reduction, that is the critical-dose rate threshold decreased. An example of this is shown in Figure S18. This may suggest that specimen cooling is not beneficial and that heating is not the mechanism behind electron beam reduction. However, this result may be convoluted with another phenomenon. The liquid nitrogen holder may act as a cold trap reducing the pressure of oxidizing species interacting with the specimen. A model previously proposed to explain the dose rate threshold in CeO_2 is a rate balance; when the reduction process is faster than the oxidation process the particle reduces, otherwise it oxidizes or maintains oxidation state (Johnston-Peck et al., 2016). If the holder is reducing the oxygen potential of the environment then the critical-dose rate threshold would decrease. However, without the appropriate tools to measure the partial pressure of oxygen and water vapor in proximity of the specimen it becomes difficult to deconvolute these two behaviors.

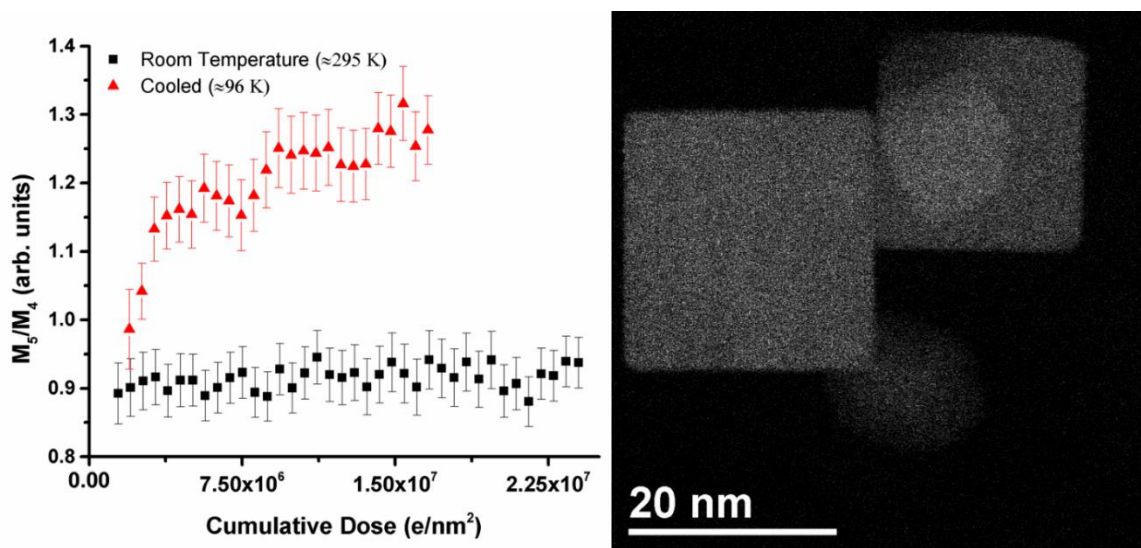


Figure S18. Oxidation state measurements from CeO_2 cubes measured with a beam current of 201 pA (dose rate of $4.66 \times 10^5 \text{ e nm}^{-2} \text{ s}^{-1}$). The measurements were acquired at ambient and liquid nitrogen temperatures while other experimental parameters were constant. Under ambient conditions the oxidation state of the particles remains unchanged but when the sample is cooled the particles reduce.

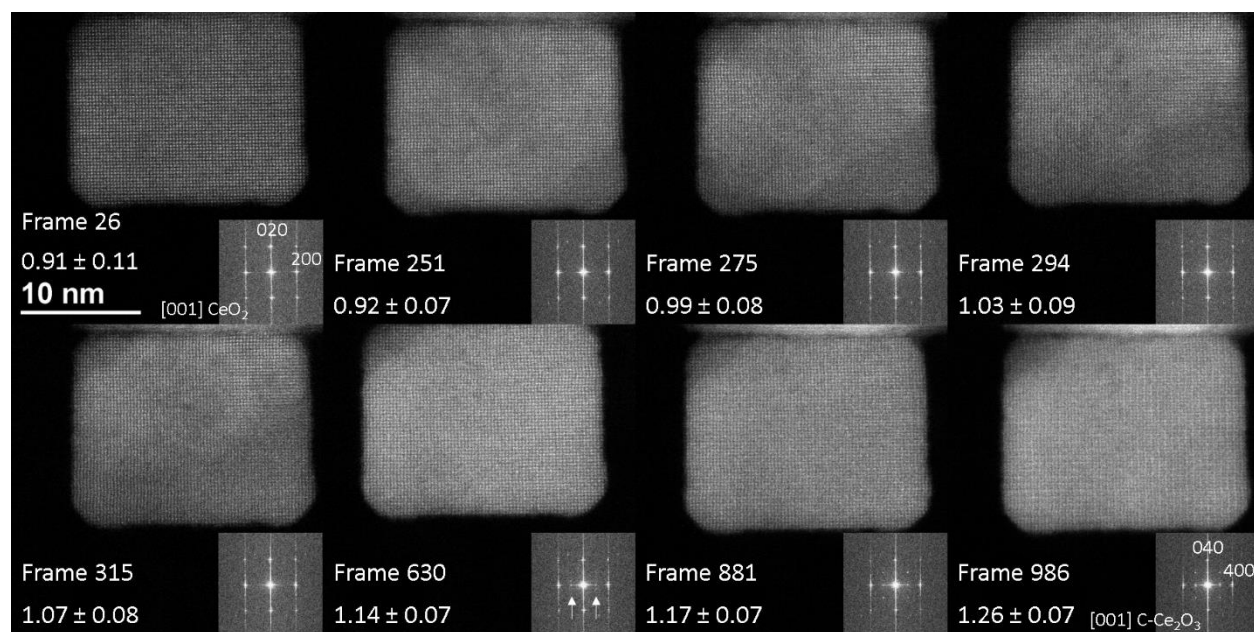


Figure S19. Figure 2 from the main text reproduced without dashed-line overlays.

Movie Information

“Cube_Redox” shows the reduction of a CeO_2 nanocube to CeO_{2-x} and then $\text{C-Ce}_2\text{O}_3$ followed by oxidation back to CeO_{2-x} and then CeO_2 . Images from this dataset were used in Figure 5. To construct the movie file the following was performed: A FFT of each image was calculated. Both the original stack of images and FFTs were binned from (1024 x 1024) pixels to (512 x 512) pixels. The stacks were then merged. The .mp4 file was generated using a H.264 codec. The frame rate is 10 fps. The original images were recorded using a dwell time of 0.8 μs which corresponds to a frame time of approximately 1s, therefore, the movie is sped up 10 times real time.

“TruncatedOctahedron_Redox” shows the reduction of a CeO_2 truncated octahedron to CeO_{2-x} followed by oxidation back to CeO_2 . Images from this dataset were used in Figure 6. To construct the movie the following was performed: An FFT of each image was calculated. Both the original stack of images and FFTs were binned from (1024 x 1024) pixels to (512 x 512 pixels). The stacks were then merged. The .mp4 file was generated using a H.264 codec. The frame rate is 10 fps. The original images were recorded using a dwell time of 0.8 μs which corresponds to a frame time of approximately 1s, therefore, the movie is sped up 10 times real time.

References

- A. Jablonski, F.S., C. J. Powell, A. Y. Lee, 2016. NIST Electron Elastic-Scattering Cross-Section Database Version 4.0, NIST Standard Reference Database Number 64. National Institute of Standards and Technology, Gaithersburg MD, 20899.
- Johnston-Peck, A.C., DuChene, J.S., Roberts, A.D., Wei, W.D., Herzing, A.A., 2016. Dose-rate-dependent damage of cerium dioxide in the scanning transmission electron microscope. *Ultramicroscopy* 170, 1-9.
- Kim, Y.-K., Irikura, K.K., Rudd, M.E., Ali, M.A., Stone, P.M., Chang, J., Coursey, J.S., Dragoset, R.A., Kishore, A.R., Olsen, K.J., Sansonetti, A.M., Wiersma, G.G., Zucker, D.S., Zucker, M.A., 2004. Electron-Impact Ionization Cross Section for Ionization and Excitation Database (version 3.0). National Institute of Standards and Technology, Gaithersburg, MD.
- Mitchell, D.R.G., Schaffer, B., 2005. Scripting-customised microscopy tools for Digital Micrograph™. *Ultramicroscopy* 103, 319-332.
- Schindelin, J., Arganda-Carreras, I., Frise, E., Kaynig, V., Longair, M., Pietzsch, T., Preibisch, S., Rueden, C., Saalfeld, S., Schmid, B., Tinevez, J.-Y., White, D.J., Hartenstein, V., Eliceiri, K., Tomancak, P., Cardona, A., 2012. Fiji: an open-source platform for biological-image analysis. *Nat Meth* 9, 676-682.
- Schneider, C.A., Rasband, W.S., Eliceiri, K.W., 2012. NIH Image to ImageJ: 25 years of image analysis. *Nat Meth* 9, 671-675.
- Thevenaz, P., Ruttimann, U.E., Unser, M., 1998. A pyramid approach to subpixel registration based on intensity. *IEEE Transactions on Image Processing* 7, 27-41.
- Verbeeck, J., Van Aert, S., 2004. Model based quantification of EELS spectra. *Ultramicroscopy* 101, 207-224.